UNIVERSITY OF AMSTERDAM

UvA-DARE (Digital Academic Repository)

IXPE observation of the low-synchrotron peaked blazar S4 0954+65 during an optical-X-ray flare

Kouch, Pouya M.; Ng, Chi-Yung; Vink, Jacco; IXPE

DOI
10.1051/0004-6361/202453127

Publication date
2025

Document Version
Final published version

Published in
Astronomy and Astrophysics

License
CC BY

Link to publication

Citation for published version (APA):
Kouch, P. M., Ng, C.-Y., Vink, J., & IXPE (2025). IXPE observation of the low-synchrotron peaked blazar S4 0954+65 during an optical-X-ray flare. *Astronomy and Astrophysics*, *695*, Article A99. https://doi.org/10.1051/0004-6361/202453127

General rights
It is not permitted to download or to forward/distribute the text or part of it without the consent of the author(s) and/or copyright holder(s), other than for strictly personal, individual use, unless the work is under an open content license (like Creative Commons).

Disclaimer/Complaints regulations
If you believe that digital publication of certain material infringes any of your rights or (privacy) interests, please let the Library know, stating your reasons. In case of a legitimate complaint, the Library will make the material inaccessible and/or remove it from the website. Please Ask the Library: https://uba.uva.nl/en/contact, or a letter to: Library of the University of Amsterdam, Secretariat, P.O. Box 19185, 1000 GD Amsterdam, The Netherlands. You will be contacted as soon as possible.

UvA-DARE is a service provided by the library of the University of Amsterdam (https://dare.uva.nl)

Download date:07 Oct 2026

A&A, 695, A99 (2025)
https://doi.org/10.1051/0004-6361/202453127
© The Authors 2025

Astronomy & Astrophysics

IXPE observation of the low-synchrotron peaked blazar S4 0954+65 during an optical-X-ray flare

Pouya M. Kouch[1,2,⋆], Ioannis Liodakis[3,4], Francesco Fenu[5], Haocheng Zhang[6,7], Stella Boula[8], Riccardo Middei[9,10], Laura Di Gesu[5], Georgios F. Paraschos[11], Iván Agudo[12], Svetlana G. Jorstad[13,14], Elina Lindfors[1], Alan P. Marscher[13], Henric Krawczynski[15], Michela Negro[16], Kun Hu[15], Dawoon E. Kim[17,18,19], Elisabetta Cavazzuti[5], Manel Errando[15], Dmitry Blinov[3,20], Anastasia Gourni[20], Sebastian Kiehlmann[3,20], Angelos Kourtidis[21], Nikos Mandarakas[3,20], Nikolaos Triantafyllou[20], Anna Vervelaki[20], George A. Borman[22], Evgenia N. Kopatskaya[14], Elena G. Larionova[14], Daria A. Morozova[14], Sergey S. Savchenko[14,23], Andrey A. Vasilyev[14], Ivan S. Troitskiy[14], Tatiana S. Grishina[14], Ekaterina V. Shishkina[14], Alexey V. Zhovtan[22], Francisco José Aceituno[12], Giacomo Bonnoli[8,12], Víctor Casanova[12], Juan Escudero[12], Beatriz Agís-González[3], César Husillos[24,12], Jorge Otero-Santos[12], Vilppu Piirola[1], Alfredo Sota[12], Ioannis Myserlis[25,11], Mark Gurwell[26], Garrett K. Keating[26], Ramprasad Rao[26], Emmanouil Angelakis[27], Alexander Kraus[11], Lucio Angelo Antonelli[10,9], Matteo Bachetti[28], Luca Baldini[29,30], Wayne H. Baumgartner[31], Ronaldo Bellazzini[29], Stefano Bianchi[32], Stephen D. Bongiorno[4], Raffaella Bonino[33,34], Alessandro Brez[29], Niccolò Bucciantini[35,36,37], Fiamma Capitanio[17], Simone Castellano[29], Chien-Ting Chen[38], Stefano Ciprini[39,9], Enrico Costa[17], Alessandra De Rosa[17], Ettore Del Monte[17], Niccolò Di Lalla[40], Alessandro Di Marco[17], Immacolata Donnarumma[5], Victor Doroshenko[41], Michal Dovčiak[42], Steven R. Ehlert[4], Teruaki Enoto[43], Yuri Evangelista[17], Sergio Fabiani[17], Riccardo Ferrazzoli[17], Javier A. Garcia[7], Shuichi Gunji[44], Kiyoshi Hayashida[45], Jeremy Heyl[46], Wataru Iwakiri[47], Philip Kaaret[4], Vladimir Karas[42], Fabian Kislat[48], Takao Kitaguchi[43], Jeffery J. Kolodziejczak[4], Fabio La Monaca[17,19,18], Luca Latronico[33], Simone Maldera[33], Alberto Manfreda[49], Frédéric Marin[50], Andrea Marinucci[5], Herman L. Marshall[51], Francesco Massaro[33,34], Giorgio Matt[32], Ikuyuki Mitsuishi[52], Tsunefumi Mizuno[53], Fabio Muleri[17], Chi-Yung Ng[54], Stephen L. O'Dell[4], Nicola Omodei[40], Chiara Oppedisano[33], Alessandro Papitto[10], George G. Pavlov[55], Abel Lawrence Peirson[40], Matteo Perri[9,10], Melissa Pesce-Rollins[29], Pierre-Olivier Petrucci[56], Maura Pilia[28], Andrea Possenti[28], Juri Poutanen[1], Simonetta Puccetti[9], Brian D. Ramsey[4], John Rankin[8], Ajay Ratheesh[17], Oliver J. Roberts[38], Carmelo Sgrò[29], Patrick Slane[26], Paolo Soffitta[17], Gloria Spandre[29], Douglas A. Swartz[38], Toru Tamagawa[43], Fabrizio Tavecchio[8], Roberto Taverna[57], Yuzuru Tawara[52], Allyn F. Tennant[4], Nicholas E. Thomas[4], Francesco Tombesi[19,39,58], Alessio Trois[28], Sergey S. Tsygankov[1], Roberto Turolla[57,59], Roger W. Romani[40], Jacco Vink[60], Martin C. Weisskopf[4], Kinwah Wu[59], Fei Xie[61,17], and Silvia Zane[59]

(Affiliations can be found after the references)

Received 22 November 2024 / Accepted 31 January 2025

ABSTRACT

The X-ray polarization observations, made possible with the Imaging X-ray Polarimetry Explorer (IXPE), offer new ways of probing high-energy emission processes in astrophysical jets from blazars. Here, we report the first X-ray polarization observation of the blazar S4 0954+65 in a high optical and X-ray state. During our multi-wavelength (MWL) campaign of the source, we detected an optical flare whose peak coincided with the peak of an X-ray flare. This optical-X-ray flare most likely took place in a feature moving along the parsec-scale jet, imaged at 43 GHz by the Very Long Baseline Array (VLBA). The 43 GHz polarization angle of the moving component underwent a rotation near the time of the flare. In the optical band, prior to the IXPE observation, we measured the polarization angle to be aligned with the jet axis. In contrast, during the optical flare, the optical polarization angle was perpendicular to the jet axis; after the flare, it reverted to being parallel to the jet axis. Due to the smooth behavior of the optical polarization angle during the flare, we favor shocks as the main acceleration mechanism. We also infer that the ambient magnetic field lines in the jet were parallel to the jet position angle. The average degree of optical polarization during the IXPE observation was $(14.3 \pm 4.1)\%$. Despite the flare, we only detected an upper limit of 14% (at 3σ level) on the X-ray polarization degree; however, a reasonable assumption on the X-ray polarization angle results in an upper limit of 8.8% (3σ). We modeled the spectral energy distribution (SED) and spectral polarization distribution (SPD) of S4 0954+65 with leptonic (synchrotron self-Compton) and hadronic (proton and pair synchrotron) models. Our combined MWL polarization observations and SED modeling tentatively disfavor the use of hadronic models for the X-ray emission in S4 0954+65.

Key words. magnetic fields – polarization – relativistic processes – BL Lacertae objects: individual: S4 0954+65 – galaxies: jets

⋆ Corresponding author; pouya.kouch@utu.fi

Open Access article, published by EDP Sciences, under the terms of the Creative Commons Attribution License (https://creativecommons.org/licenses/by/4.0), which permits unrestricted use, distribution, and reproduction in any medium, provided the original work is properly cited.
This article is published in open access under the Subscribe to Open model. Subscribe to A&A to support open access publication.

1. Introduction

Blazars are active galactic nuclei (AGNs) with relativistic jets aligned within a small viewing angle toward an observer. These powerful objects are observed through the entire electromagnetic spectrum from radio to very-high-energy (VHE; 100 GeV to 100 TeV) γ-rays. Their energy output at almost all wavelengths exhibits rapid, seemingly stochastic variations (e.g., Ulrich et al. 1997). Conventionally, blazars are classified into two subgroups: BL Lac objects (BLLs), with largely featureless optical spectra, and flat spectrum radio quasars (FSRQs), which exhibit strong emission lines. Spectral energy distributions (SEDs) of blazars typically exhibit a double-humped structure. It is generally accepted that the low-energy component of a blazar SED arises due to the synchrotron emission of electrons and positrons radiating in the magnetized jet. Based on the peak frequency of this synchrotron component ($\nu_{\rm Sy}$), blazars have been further subdivided into low-, intermediate-, and high-synchrotron peaked sources (e.g., Abdo et al. 2010): LSP ($\nu_{\rm Sy} < 10^{14}$ Hz), ISP ($10^{14} < \nu_{\rm Sy} < 10^{15}$ Hz), and HSP ($\nu_{\rm Sy} > 10^{15}$ Hz). For recent reviews of blazar studies, we refer to Böttcher (2019), Blandford et al. (2019), and Hovatta & Lindfors (2019).

The origin of the high-energy component of blazar SEDs is still not fully understood. Possibilities include the commonly adopted leptonic models, which explain the high-energy emission as Compton scattering. In these models, the same electrons whose synchrotron emission produces the low-energy SED component upscatter their own synchrotron photons or photons from external sources to higher energies. The former models are referred to as synchrotron self-Compton (SSC; e.g., Jones et al. 1974; Maraschi et al. 1992), while the latter are referred to as external Compton (EC; e.g., Dermer et al. 1992; Sikora et al. 1994). On the other hand, hadronic emission models invoke synchrotron emission by protons or secondary particles produced in photo-pion cascades, to explain the origin of the high-energy component of blazar SEDs (e.g., Mannheim & Biermann 1989). Hadronic emission models are typically less favored than leptonic ones (e.g., Böttcher et al. 2013), since, for them to be efficient, the total energy requirement in protons is often unsustainably large. It can sometimes be even higher than the Eddington luminosity, since a large fraction of protons must reach energies $\gtrsim$ PeV to exceed the photo-pion energy threshold (e.g., Boettcher et al. 2022). Additionally, hadronic models require rather high magnetic field strengths (~10–300 G, e.g., Liodakis & Petropoulou 2020). Nevertheless, the recent ~3σ spatio-temporal association of the blazar TXS 0506+056 with high-energy neutrinos detected by the IceCube Neutrino Observatory (IceCube Collaboration 2018), coupled with the possibility that there may be a population-based correlation between high-energy neutrinos and blazars (or at least a subpopulation of blazars; e.g., Padovani et al. 2016; Kouch et al. 2024a), suggests that hadronic processes may be important in blazar jets (e.g., Petropoulou et al. 2020).

Given the inherent differences in the polarization properties of electron synchrotron, proton synchrotron, and Compton radiation, multi-wavelength (MWL) polarization measurements are crucial for distinguishing between different particle acceleration and emission models for blazar jets (e.g., Marscher et al. 2008). Linear polarization is typically represented via two quantities derived from the Stokes parameters (Q, U, and I)[1]: the polarization degree ($\Pi = \sqrt{Q^2 + U^2}/I$) and the polarization angle ($\Psi = \frac{1}{2}\arctan\left[\frac{U}{Q}\right]$). The former measures the net fraction of the incoming radiation that is linearly polarized, while the latter is the direction of the linear polarization electric vector on the sky. In blazars, the polarization degree of synchrotron radiation ($\Pi_{\rm Sy}$) ranges from zero to as high as ~50% (e.g., Mead et al. 1990) and generally indicates how ordered the magnetic field lines are in the emission region. Both electron and proton synchrotron radiation are expected to yield a high degree of polarization if the magnetic field is not very disordered. One way to distinguish them is by measuring the variability of $\Pi_{\rm Sy}$, since that of the proton synchrotron is expected to be more stable due to the longer proton cooling times compared to electrons and positrons (Zhang et al. 2016).

On the other hand, while Compton scattering does not inherently lead to polarized radiation, it can do so depending on the polarization of the seed photons and the anisotropy of the upscattering particles. In SSC, since the seed photons are polarized, $\Pi_{\rm SSC}$ is expected to be non-zero but still much smaller than $\Pi_{\rm Sy}$ ($\Pi_{\rm SSC}/\Pi_{\rm Sy} \sim 0.3$; e.g., Bonometto & Saggion 1973; Poutanen 1994; Krawczynski 2012; Peirson & Romani 2019). In EC, while the seed photons are thermal and unpolarized, the upscattering electrons may be relatively cold and exhibit extreme anisotropy with respect to the seed photons, which could result in a sizable value of $\Pi_{\rm EC}$ (e.g., Begelman & Sikora 1987). Alternatively, if such anisotropy does not exist, then $\Pi_{\rm EC}$ is expected to be very small (<1%; e.g., Bonometto et al. 1970; Krawczynski 2012).

Such contrasts between the polarization properties of the various emission models mean that contemporaneous MWL polarization measurements can serve as powerful diagnostic tools for constraining emission and acceleration models, as well as the magnetic field strength and morphology in blazar jets, especially when probing higher-energy bands, such as X-rays and γ-rays (e.g., Zhang & Böttcher 2013; Zhang et al. 2019). Notably, in HSP blazars the peak of the low-energy (synchrotron) component falls close to the X-ray regime; hence, HSP sources are expected to show a high degree of polarization in the X-ray band. This expectation was confirmed with the advent of the Imaging X-ray Polarimetry Explorer (IXPE, Weisskopf et al. 2022), which has opened a new window of polarimetric measurements to the X-ray universe (2–8 keV; e.g., Ehlert et al. 2022); the highest detected $\Pi_{\rm X}$ thus far is 31%, in the HSP blazar PKS 2155−304 (Kouch et al. 2024b). Altogether, MWL campaigns of several HSP sources conducted contemporaneously by the IXPE collaboration have revealed a general pattern: while there is a lack of correlation between the MWL polarization properties, the polarization degree in the X-ray band is on average greater than that in the optical band, which is itself (on average) greater than that in the radio band (i.e., $\Pi_{\rm X} > \Pi_{\rm O} \gtrsim \Pi_{\rm R}$). This favors acceleration at a shock front as the most likely scenario of particle energization in the jets of HSP sources, with energy stratification in the region beyond the front where the particles lose energy to radiation and adiabatic expansion (e.g., Marscher & Gear 1985; Liodakis et al. 2022b; Di Gesu et al. 2022a, 2023; Middei et al. 2023a; Ehlert et al. 2023; Kim et al. 2024; Kouch et al. 2024b; Chen et al. 2024). On the other hand, in the case of one HSP source, 1ES 1959+650, it exhibited greater variability than could be resolved by IXPE and the aforementioned trend was not detected (Errando et al. 2024).

In LSP and ISP sources, the X-ray regime generally probes the high-energy component or a mix of the low-energy and high-energy components of the blazar emission. Thus, a sizable $\Pi_{\rm X}$

[1] Another Stokes parameter V measures circular polarization, which is intrinsically small in blazars ($\lesssim$1%; Liodakis et al. 2022a, 2023). It is usually ignored and not measured by IXPE at all. When including V, the polarization degree is $\Pi = \sqrt{Q^2 + U^2 + V^2}/I$).

(i.e., $\Pi_X \gtrsim \Pi_O$) could suggest that hadronic processes play a key role in the high-energy emission of blazars or that the majority of the high-energy emission can be explained by the anisotropic-EC scenario. On the other hand, a low value of Π_X (i.e., $\Pi_X \sim 0.3 \times \Pi_O$) in LSPs and ISPs would suggest that their high-energy component is dominated by SSC. Likewise, $\Pi_X \sim 0$ would strongly favor an EC or SSC dominated emission process where the relativistically moving plasma does not contain relatively cold electrons. The IXPE observations of the blazar BL Lacertae (an LSP-ISP source) in LSP-like states measured $\Pi_X < 12.6\%$ (at 99% confidence level) and demonstrated that $\Pi_X < \Pi_O$ (Middei et al. 2023b). Meanwhile, during an ISP-like state when the X-ray photons were coming from the low-energy (synchrotron) component, an IXPE observation of BL Lacertae resulted in $\Pi_X \sim 22\% > \Pi_O$ in the limited energy range of 2–4 keV (Peirson et al. 2023). The IXPE observations of other LSP-ISP sources (three LSPs and one ISP) have only resulted in upper limits of $\Pi_X < 9\%$ to $\Pi_X < 28\%$ (at 99% confidence levels; Marshall et al. 2024). Therefore, while these results are not conclusive enough to completely exclude the presence of some hadronic processes in blazar jets, they strongly disfavor purely hadronic (e.g., pure proton synchrotron) and anisotropic-EC scenarios.

In this paper, we present the results of a MWL campaign of the IXPE collaboration on the LSP blazar S4 0954+65 during an optical-X-ray flaring episode. S4 0954+65 has J2000 sky coordinates of RA = 149.697083° and Dec = 65.565278° at a redshift of 0.3694 ± 0.0011 (Lawrence et al. 1986; Becerra González et al. 2021). It is known to frequently exhibit high polarization and flaring behavior in the optical band. It was identified among the prime targets for IXPE to distinguish between leptonic and hadronic scenarios (Liodakis et al. 2019). S4 0954+65 is generally classified as a BLL due to its rather weak emission lines (Ghisellini et al. 2011). Nevertheless, the features of its SED somewhat resemble those of an FSRQ, which suggests that S4 0954+65 may be a transitional object between the two classes (Becerra González et al. 2021). S4 0954+65 is a known emitter of GeV and VHE γ-rays (Mukherjee et al. 1995; Krauss 2014; MAGIC Collaboration 2018). Photometric observations of this source have found long-term variability in both the radio and optical bands (with the former lagging behind the latter by ∼3 weeks), which was interpreted to arise from dynamical rotation of the jet that gradually alters the beaming angle with respect to our line of sight (e.g., Raiteri et al. 1999, 2021, 2023). Timescale analyses by Sharma et al. (2024) of the 15-year-long *Fermi*-LAT light curves of S4 0954+65 have led to the speculation that the data indicate disc-jet coupling. Furthermore, both photometric and polarimetric observations of S4 0954+65 have shown rapid variability in both the radio and optical bands (e.g., Gabuzda et al. 2000; Marchili et al. 2012; Bachev 2015; Raiteri et al. 2021, 2023; Pandey et al. 2023).

Morozova et al. (2014) observed S4 0954+65 as part of a MWL campaign in 2011. They performed optical photometry and polarimetry measurements, as well as Very Long Baseline Array (VLBA) imaging of the source, and utilized *Fermi* γ-ray flux density measurements in their study. Between January and March, the optical brightness of S4 0954+65 increased by ∼3 mag. Between March and April 2011, they observed several optical-γ-ray flares, accompanied by smooth rotations of the optical polarization angle (Ψ_O). On the night of March 9, S4 0954+65 exhibited an extremely fast optical-γ-ray flare (its optical brightness increased by ∼0.7 mag within 7 h); this occurred along with a smooth 300° rotation in Ψ_O. This was likely associated with the ejection of an apparently superluminal (∼19 c) knot from the compact "core" of S4 0954+65. Furthermore, they analyzed other optical flares between 2008 and 2012, finding similar connections between optical variability and the ejection of superluminal knots from the core. Notably, they found that S4 0954+65 generally shows pronounced optical variability (both in flux and polarization properties). Interestingly, they also determined that S4 0954+65 tends to eject around three superluminal knots per year, similar to the rate of optical flares.

The MAGIC Collaboration (2018) conducted a MWL campaign on S4 0954+65 in February 2015, when it was experiencing a major flare from radio to VHE γ-rays. They interpreted the flare to be caused by a relativistic plasma blob (detected in high-resolution 43 GHz maps of the compact core) propagating in a helical magnetic field and crossing a standing shock. This event was accompanied by an optical polarization angle rotation of ∼100°. They modeled the high-energy emission by invoking EC models where the IR seed photons originate from a luminous dusty torus. Similarly, Deng et al. (2022) showed that EC models could still explain the observed SED of the source even when using far more energetic seed photons, possibly coming from a putative broad-line region (Becerra González et al. 2021) residing closer to the central engine than the dusty torus. Other studies invoked a combination of SSC and EC models. For example, the significant hardening of the spectrum at GeV energies and the softening at keV energies during this major flaring episode in 2015 were interpreted by Tanaka et al. (2016) as favoring SSC models, although they used a one-zone, dusty-torus-driven EC model to explain the GeV-TeV portion of the SED.

Raiteri et al. (2023) conducted a high-cadence photometric and polarimetric monitoring campaign on S4 0954+65 in the optical band during another major flaring episode (April-May 2022). They detected an extremely short variability timescale of 17 minutes, and used it to estimate the size of the emission region to be on the order of 10^{-4} pc. They linked such fast, bluer-when-brighter variability patterns to SSC processes present in the jet of the source. Additionally, they found that the variations of the polarization properties in the optical band were more extreme than the radio band, but the average optical polarization angle (Ψ_O) and radio polarization angle (Ψ_R) remained similar. During this flaring period, on April 13, 2022, Pandey et al. (2023) detected a 120° polarization angle rotation within a 3 hour period in the optical band. They also measured a change as large as ∼10% in the optical polarization degree of the source within one day. Additionally, they observed that, from mid-March to the end of April 2022, S4 0954+65 reached minimum and maximum values of Π_O of 3% and 39%, respectively. In this period, the range of Ψ_O was 11° to 169°. Notably, no correlation between the optical flux density and Π_O variations was found (Raiteri et al. 2021; Pandey et al. 2023).

Milliarcsecond-scale (mas) very-long-baseline interferometry (VLBI) maps of S4 0954+65 in the 5 and 8 GHz bands in the 1990s revealed a bright, compact "core," plus a jet pointing west-northwest, bending with distance to point almost directly westward (i.e., $-90° \lesssim \Psi_{jet,5} \lesssim -70°$)[2] 3–5 mas from the core (Gabuzda et al. 2000). 15 GHz VLBI maps of S4 0954+65, as part of the Monitoring Of Jets in Active galactic nuclei with VLBA Experiments (MOJAVE[3]) program between the years 1995 and 2013, revealed the jet to point in the general northwest direction on mas scales ($-60° \lesssim \Psi_{jet,15} \lesssim -30°$; Hovatta et al. 2014; Lister et al. 2018). In 43 GHz VLBA images on sub-

[2] Position angles are measured from north through east.
[3] https://www.cv.nrao.edu/MOJAVE/sourcepages/0954+658.shtml

mas scales between 2010 and 2018, the jet was in the north-northwest direction ($-30° \lesssim \Psi_{\rm jet,43} \lesssim -10°$; Jorstad et al. 2017; MAGIC Collaboration 2018; Weaver et al. 2022). The most recent 43 GHz VLBA maps of the source[4] suggest that the parsec-scale jet of S4 0954+65 still pointed toward the general north-northwest direction throughout 2023 (for more details, see Sect. 3.3).

We describe the X-ray and the accompanying contemporaneous MWL observations of S4 0954+65 in Sects. 2 and 3, respectively. We explain the process used to theoretically model the emission of the source in Sect. 4. Finally, we summarize the results and discuss them in the context of leptonic and hadronic models in Sect. 5.

2. X-ray observations and analysis methods

2.1. IXPE observations

IXPE observed S4 0954+65 between May 25, 2023 (MJD 60089) and June 03, 2023 (MJD 60098) with a total exposure time of about 490 ks. We remove the instrumental background following the rejection strategy of Di Marco et al. (2023) and we use the `ixpeobssim` software (Baldini et al. 2022) to analyse the data. The source events are extracted within a circular region (radius of 1.1 arcmin) centered on the source, while the background events are determined using an annulus with inner and outer radii of 2.0 and 5.0 arcmin, respectively, centered on the source. Figure 1 shows the light curve of the source in the 2–8 keV range obtained using the `LC` algorithm of `ixpeobssim`. The source exhibits a flare between MJD 60094 and 60096 with a peak at MJD 60095 (i.e., 2023 May 31).

We determined the polarization properties (in the 2–8 keV energy regime) using the procedure described in Kislat et al. (2015), which is implemented in the `PCUBE` algorithm of `ixpeobssim`. Additionally, we obtained the 2–8 keV polarization properties using a spectro-polarimetric fit. The two procedures return consistent results within uncertainties. Henceforth, we focus only on the results of the spectro-polarimetric fit. The energy spectrum was obtained from the `PHA1` algorithm of `ixpeobssim`, while `PHA1Q` and `PHA1U` were used to derive spectra for each of the Stokes parameters. Following Di Marco et al. (2022), a weighted analysis was employed to improve the sensitivity. For the total energy spectrum (I-spectrum), the bins were merged with `ftgrppha` of `ftools` until a signal-to-noise ratio (S/N) of at least 5 is reached. For the spectra of the Stokes parameters (Q- and U-spectra), a binning was chosen to guarantee at least five counts in each bin. The spectro-polarimetric fit is performed via `Xspec`. To account for the Galactic absorption, we used the Tuebingen-Boulder model (`tbabs` in `Xspec`) with an n_H column density of 4.68×10^{20} cm^{-2} (Dickey & Lockman 1990). We fit the data with a power law model (`powerlaw`) multiplied by an energy-independent polarization (`polconst`).

We did not detect X-ray polarization ($\Pi_{\rm X}$) of S4 0954+65 at a 3σ confidence level. When taking the entire IXPE observation window into account, we obtained an upper limit (99.73% confidence level) of $\Pi_{\rm X} < 14\%$. In an attempt to improve the constraints on $\Pi_{\rm X}$, we reduced the number of free parameters involved in the spectro-polarimetric fit by assuming a number of physical scenarios: we fix the X-ray polarization angle ($\Psi_{\rm X}$) to be either parallel or perpendicular to the jet position angle ($\Psi_{\rm jet,43} = -42° \pm 7°$, see Sect. 3.3) or to the measured optical polarization angle ($\Psi_{\rm O} = 66.5°$, see Sect. 3.3). Additionally, we consider three time intervals: the full IXPE exposure (from MJD 60089 to 60098); the interval in which the optical polarization angle appears to stay constant (MJD 60092 to 60095, see Sect. 3); and the period during which the X-ray flux peaks (as detected by IXPE, from MJD 60094 to 60096; see Fig. 1). The results of these tests are presented in Table 1. A scenario under which $\Psi_{\rm X}$ is roughly perpendicular to the constant value of $\Psi_{\rm O}$ yields the strongest constraints on the X-ray polarization degree, $\Pi_{\rm X} < 8.4\%$ (at 99.73% confidence level). Notably, when $\Psi_{\rm X}$ is perpendicular to the jet position angle, we obtained $\Pi_{\rm X} < 8.8\%$ (at a 99.73% confidence level). We emphasize that fixing other

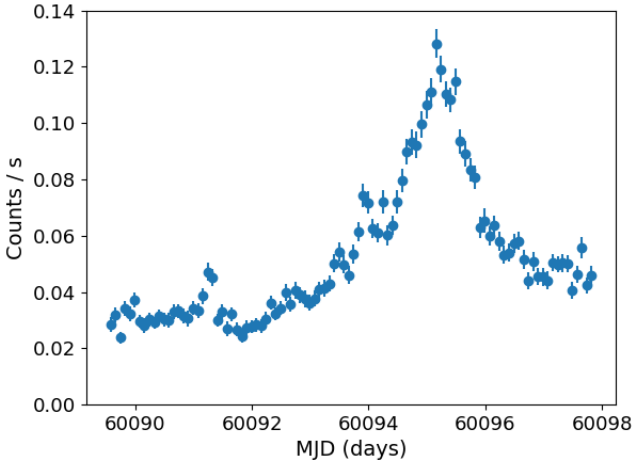

Fig. 1. X-ray photon counts from S4 0954+65 as detected by IXPE plotted against time (MJD). IXPE observed the source from MJD 60089 until 60098. The X-ray flux experiences several minor flares and a major one. In this paper, we focus on the major flare which occurs approximately from MJD 60094 to 60096 (peaking at MJD 60095, 2023 May 31).

Table 1. Upper limits (99% and 99.73% confidence levels) to the X-ray polarization angle ($\Psi_{\rm X}$) and degree ($\Pi_{\rm X}$) as calculated via the spectro-polarimetric fit for different alignment scenarios.

T (1)	$\Psi_{\rm X}$ alignment (2)	Fixed $\Psi_{\rm X}$ (3)	$\Pi_{\rm X,99\%}$ (4)	$\Pi_{\rm X,99.73\%}$ (5)
Full	$\Psi_{\rm X} \parallel \Psi_{\rm jet,43}$	$-42° \equiv 138°$	<9.8%	<11%
	$\Psi_{\rm X} \perp \Psi_{\rm jet,43}$	$48° \equiv -132°$	<7.4%	<8.8%
	–	(not fixed)	<13%	<14%
	$\Psi_{\rm X} \parallel \Psi_{\rm O}$	$66.5° \equiv -113.5°$	<10%	<11%
	$\Psi_{\rm X} \perp \Psi_{\rm O}$	$156.5° \equiv -23.5$	<7.0%	<8.4%
Const.	–	(not fixed)	<20%	<22%
	$\Psi_{\rm X} \parallel \Psi_{\rm O}$	$66.5° \equiv -113.5°$	<8.1%	<9.9%
	$\Psi_{\rm X} \perp \Psi_{\rm O}$	$156.5° \equiv -23.5$	<17%	<19%
Peak	–	(not fixed)	<13%	<15%
	$\Psi_{\rm X} \parallel \Psi_{\rm O}$	$66.5° \equiv -113.5°$	<12%	<14%
	$\Psi_{\rm X} \perp \Psi_{\rm O}$	$156.5° \equiv -23.5$	<11%	<13%

Notes. Columns: (1) time interval used in the spectro-polarimetric analysis; (2) alignment used to fix the value of the X-ray polarization angle ($\Psi_{\rm X}$); (3) fixed value of $\Psi_{\rm X}$; (4) upper limit to X-ray polarization degree at 99% confidence level; (5) upper limit to X-ray polarization degree at 99.73% confidence level (i.e., Gaussian 3σ). "Full" refers to the entire IXPE observing period (MJD 60089-60098); "Const." refers to the constant $\Psi_{\rm O}$ period (MJD 60092-60095), and "Peak" refers to the period in which the IXPE flux peaked (MJD 60094-60096; see Fig. 1). In column (3), the symbol "≡" is used to represent the inherent ±180° ambiguity in the polarization angles.

[4] https://www.bu.edu/blazars/VLBA_GLAST/0954.html

values of Ψ_X typically has a minimal effect on the Π_X upper limits. Generally, we obtained less constraining upper limits when the shorter time bins are considered.

Since the source exhibits a flare during the IXPE observation, we inspect the data for spectral variability during the observation. All photon spectral index measurements, as calculated with the spectro-polarimetric fit, are consistent with a constant value of $\Gamma = 1.69 \pm 0.03$. Similarly, all hardness ratio measurements, defined as $(\phi_{low} - \phi_{high})/(\phi_{low} + \phi_{high})$ with ϕ_{low} and ϕ_{high} being the photon count rates in the 2–4 and 4–8 keV intervals, respectively, remain consistent with a constant value of 0.71 ± 0.01 throughout the IXPE observation. This indicates that the source did not experience any significant spectral variations. Therefore, we checked for variability in polarization by splitting the IXPE data into both equal and variable time intervals. To obtain the polarization properties in this test, we used both the spectro-polarimetric fit and the `PCUBE` algorithm. No X-ray polarization was detected in any of the selected time intervals via either of the two methods. Lastly, to check for energy dependence, we divided the IXPE data into two ranges: 2–4 and 4–8 keV. We then applied the spectro-polarimetric fit to both separately, using an energy-independent polarization model (`polconst` in `Xspec`). We did not find any significant polarization in either of the two energy bins, as Π_X upper limits (at the 3σ level) are >20% in all of the tests.

2.2. XMM-Newton

The *XMM-Newton* space observatory (Jansen et al. 2001) targeted S4 0954+65 from 2023 May 20 (22:41:00 UT) to May 21 (01:44:53 UT) for a net exposure time of 7.7 ks (Obs. ID 0920901901). The standard routines of the `SAS` (Science Analysis System, Version 21.0.0) and the latest calibration files are used to calibrate and extract the third-level science products. The background is determined from a circular region with a 40 arcsec radius centered on a source-free area of the CCDs. Then, a circular region with a radius of 22 arcsec is adopted to extract the spectrum of S4 0954+65. This radius is selected based on an iterative process aimed at maximizing the signal-to-noise ratio in the 0.3 to 10 keV regime (e.g., Piconcelli et al. 2004). We subsequently binned the obtained spectrum to have at least 30 counts per bin, while making sure to avoid oversampling the instrumental energy resolution by a factor larger than 3.

We modeled the European Photon Imaging Camera pn-CCD (EPIC-pn; Strüder et al. 2001) spectrum with an absorbed, pegged power law (`tbabs*pegpwrlw`). Additionally, since it is known that there is a strong correlation between the photon index and the absorption parameter, we fixed the value of the Galactic hydrogen absorption to $N_{H,Gal} = 4.68 \times 10^{20}$ cm^{-2} (HI4PI Collaboration 2016). We calculated the C-statistics (Cash 1979) of the fit and, to assess the goodness of the fit, we additionally computed the theoretical C-statistics as well as its variance, following Kaastra (2017). The best-fit result is given in Appendix A.

2.3. Swift-XRT

During the IXPE observation, we also observed S4 0954+65 using the X-ray Telescope (XRT) on board the space-borne *Neil Gehrels Swift* Observatory (*Swift*-XRT; see Gehrels et al. 2004) in photon-counting mode. Data taken with *Swift*-XRT is reduced and extracted following the standard procedures, using `xrtpipeline` (Version 0.13.7) and `HEASOFT` (Version 6.30). We calculated the photon flux and spectrum from a circular region centered on the source with a radius of 35 arcsec. The background events were extracted using an annulus centered on the source with inner and outer radii of 50 and 150 arcsec, respectively. The spectra were binned such that each bin contained at least one photon and they were individually fit using C-statistics (Cash 1979). To include the foreground absorption of the interstellar medium, we use `vern` cross sections (Verner et al. 1996) and `wilm` abundances (Wilms et al. 2000). We fit the data with the same model as described for the *XMM-Newton* spectrum. The best-fit results are given in Appendix A.

3. Radio, optical, and γ-ray observations

3.1. Optical and radio data

Contemporaneous with the IXPE observations, S4 0954+65 was also observed in the radio and optical bands using the Alhambra Faint Object Spectrograph and Camera (ALFOSC) at the Nordic Optical Telescope (NOT), the Effelsberg 100-m telescope (Kraus et al. 2003), the LX-200 telescope operated by St. Petersburg State University, RoboPol at the Skinakas Observatory (Ramaprakash et al. 2019), the T90 telescope at the Sierra Nevada Observatory (SNO), and the Submillimeter Array (SMA, Ho et al. 2004). Details on the data analysis and observing strategy for these MWL observations can be found in Liodakis et al. (2022b), Middei et al. (2023b), Di Gesu et al. (2023), Kouch et al. (2024b).

The Effelsberg observations were obtained as part of the Monitoring the Stokes Q, U, I and V Emission of AGN jets in Radio (QUIVER) program (Myserlis et al. 2018), and performed at 4.8, 10, and 17 GHz. The SMA observations were obtained at 225.5 GHz within the SMA Monitoring of AGNs with POLarization (SMAPOL) program (Marrone & Rao 2008; Myserlis 2024). In the B, V, R, and I optical bands (λ_{eff} of 445, 551, 658, and 806 nm, respectively), NOT provided polarimetric observations (for analysis details see, e.g., Hovatta et al. 2016; Nilsson et al. 2018). Moreover, LX-200, RoboPol, and SNO provided R-band polarimetric observations. Additionally, SNO provided photometry in R-band, and LX-200 in both R- and I-bands. We also have optical photometry data from two all-sky surveys via performing forced-photometry at the coordinate of S4 0954+65: r-band data ($\lambda_{eff} = 637$ nm) from the Zwicky Transient Facility (ZTF[5]; Bellm et al. 2019) and o-band ($\lambda_{eff} = 578$ nm) data from the Asteroid Terrestrial-impact Last Alert System (ATLAS[6]; Tonry et al. 2018) all-sky survey. In Appendix B, the optical photometric (in magnitudes) and polarimetric measurements of S4 0954+65 are given in Tables B.1 and B.2, while Table B.3 summarizes the polarimetric observations of the source made in the radio bands. The time dependence of the contemporaneous MWL polarization measurements of S4 0954+65 is shown in Fig. 2.

For about one month prior to the IXPE observations of S4 0954+65, the optical brightness was stable at ∼14.5 mag, as observed by T90 (see Table B.1). However, during the IXPE observation (MJD 60089-60098), S4 0954+65 exhibited a flare in all of the observed optical bands, with its R-band brightness rising from ∼14.5 mag to ∼13.2 mag from MJD 60092 to 60095. During the entire IXPE pointing, the optical polarization degree (Π_O) and angle (Ψ_O) were significantly variable, which is similar to the past behavior of S4 0954+65 (e.g., Raiteri et al. 2023; Pandey et al. 2023). For example, during this 1 mag optical flare, Π_O rose from ∼6% to ∼20%. During the entire IXPE

[5] https://irsa.ipac.caltech.edu/Missions/ztf.html
[6] https://fallingstar-data.com/

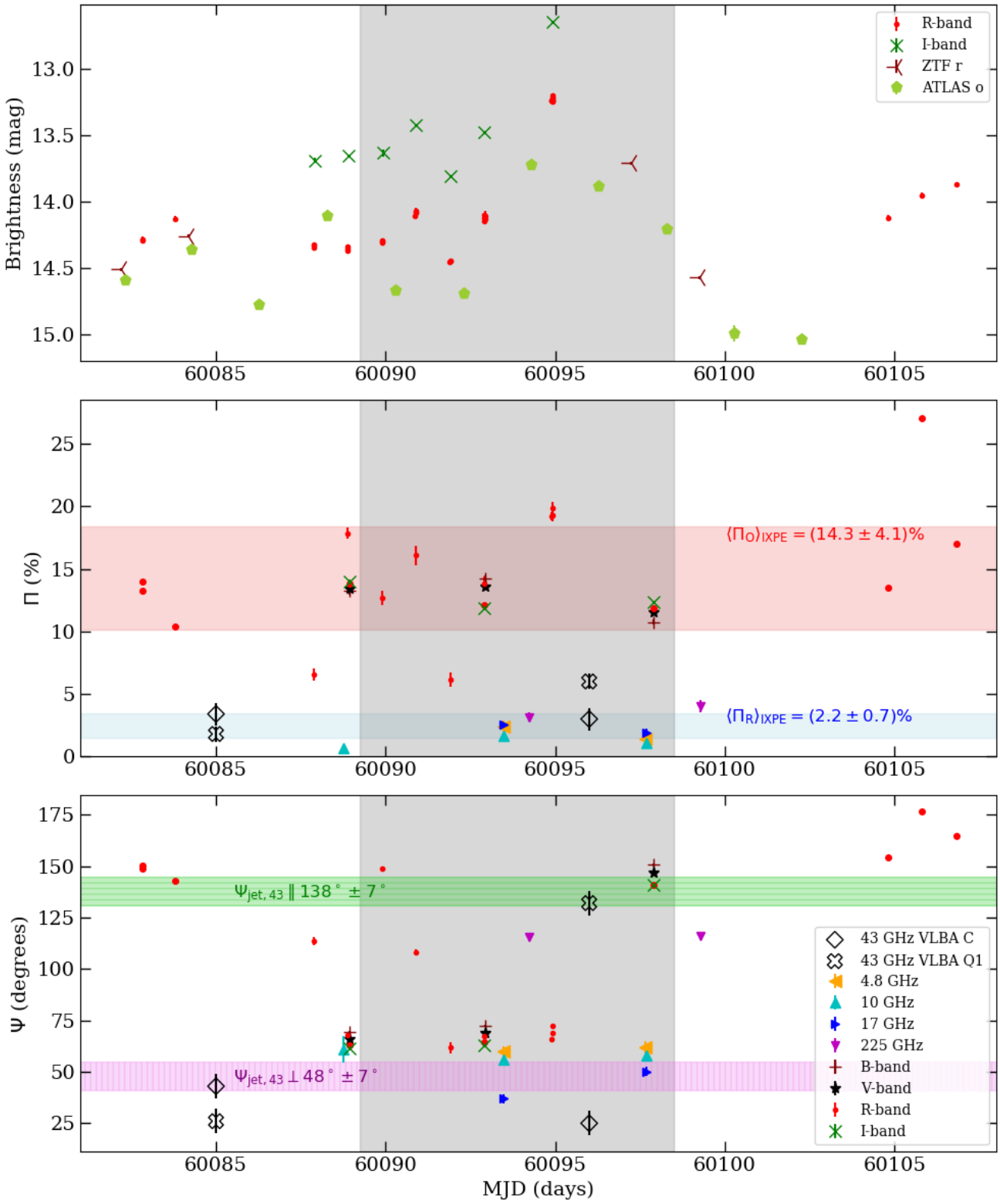

Fig. 2. Contemporaneous radio and optical observations of S4 0954+65. From top to bottom, the panels show optical brightness in magnitudes, polarization degree (Π) in %, and polarization angle (Ψ) in degrees. The grey shaded area (vertical) marks the duration of the IXPE observation (MJD 60089-60098). In the middle panel, the red and blue shaded areas (horizontal) are centered on the average Π_O and Π_R within the IXPE observation time window, respectively; the thickness of these red and blue horizontally shaded areas corresponds to the standard deviation of Π_O and Π_R within the IXPE observation time window, respectively. In the bottom panel, we indicate the parallel and perpendicular alignment directions of the jet position angle (after shifting $\Psi_{jet,43} = -42° \pm 7°$ by 180° to account for the inherent 180° ambiguity in polarization angle estimates; see Sect. 3.3) using the green and purple horizontally shaded areas, respectively. The 43 GHz VLBA C and Q1 data points refer to the polarization degree and angle of the two parsec-scale components detected at 43 GHz (see Sect. 3.3).

pointing, Π_O fluctuated about an average of 14.3% with a standard deviation of 4.1%. Meanwhile, Ψ_O varied from 62° just before the start of the IXPE observation, to 149° ($\Delta\Psi_O \approx 85°$) within one day. Right after this fast rotation, Ψ_O returned to 66.5° ($\Delta\Psi_O \approx 87°$ within 2 d) and remained constant for about 3 d (coinciding with the 1 mag flare). By the end of the IXPE observation (MJD 60098), Ψ_O returned to ∼140° and, a few days later, to ∼170°. We note that, five days prior to the IXPE pointing, Ψ_O was ∼150°. Since the 43 GHz parsec-scale jet of S4 0954+65 points toward the northwest direction ($\Psi_{jet,43} = -42° \pm 7°$; see Sect. 3.3), the temporal behavior of the optical polarization angle can be summarized roughly in the following manner (also see Fig. 2):

- MJD 60084: $\Psi_O \parallel \Psi_{jet,43}$ (followed by a rotation over 5 d);
- MJD 60089: $\Psi_O \perp \Psi_{jet,43}$ (followed by a rotation in 1 d);
- MJD 60090: $\Psi_O \parallel \Psi_{jet,43}$ (followed by a rotation over 2 d);
- MJD 60092: $\Psi_O \perp \Psi_{jet,43}$ (stayed constant for 3 d);
- MJD 60095: $\Psi_O \perp \Psi_{jet,43}$ (followed by a rotation over 3 d);
- MJD 60098: $\Psi_O \parallel \Psi_{jet,43}$ (stayed constant for at least 9 d).

At the low radio frequencies (4.8, 10, and 17 GHz), the degree of polarization of S4 0954+65 during and near the IXPE observation window was low ($1\% < \Pi_{\leq 17} < 3\%$), with a polarization angle $37° < \Psi_{\leq 17} < 60°$ (i.e., $\Psi_{\leq 17} \perp \Psi_{jet,43}$, roughly). At 225.5 GHz, the polarization degree was slightly higher ($3\% < \Pi_{225} < 4\%$), with a polarization angle $\Psi_{225} = 116° \pm 2°$. Over the course of this MWL campaign, we do not find any significant variability in the polarimetric properties of S4 0954+65 in the radio bands. Hence, during the 1 mag optical flare mentioned above (MJD 60092-60095), Π_R remained stable below 3%, and Ψ_R was essentially parallel to the constant Ψ_O of $66.5° \equiv -113.5°$ and perpendicular to the jet position angle. The lack of variability in the radio polarimetric properties as compared to those of the optical band is in line with the previous observations of S4 0954+65 (Raiteri et al. 2023).

3.2. Fermi γ-ray data

Using data from the Large Area Telescope (LAT) instrument on board the *Fermi* Gamma-ray Space Telescope (Abdollahi et al. 2020), we obtain γ-ray flux measurements of S4 0954+65 contemporaneous with the IXPE observation. These fluxes are incorporated into the modeling of the spectral energy distribution of S4 0954+65 (see Sect. 4). To obtain the γ-ray fluxes, we employ standard analysis tools (Pass8 `P8R3_source`, FERMITOOLS v.1.2.23) to select events in the 100 MeV to 300 GeV energy range. We apply the recommended zenith angle cut (90°) to avoid contamination from Earth's limb and include the diffuse and isotropic background components[7] to extract the source spectrum via a binned likelihood analysis, assuming a power-law spectrum in each bin. During this analysis, we simultaneously fit the spectrum and normalization of all the sources within the region of interest (ROI), while all sources within 10° from the ROI were fixed to the 4FGL-DR2 catalogue parameters (Ballet et al. 2020). In Table B.4 we present the spectral flux density values obtained in the *Fermi* γ-ray band.

3.3. VLBI images of S4 0954+65 near the IXPE observation

As part of the Blazars Entering the Astrophysical Multi-Messenger Era monitoring program (BEAM-ME, successor to the VLBA-BU-BLAZAR program, which ran from 2007 to 2020), S4 0954+65 was observed by the VLBA at 43 GHz during and near the IXPE observation window. Figure 3 presents four milliarcsec-scale maps of the compact region of the source at a resolution of ∼0.1 mas (for more details see Jorstad & Marscher 2016; Jorstad et al. 2017; Weaver et al. 2022). For a redshift of 0.3694 (see Sect. 1), a Hubble constant of 70 km s^{-1} Mpc^{-1}, a matter density parameter of $\Omega_m = 0.3$, and assuming a flat Universe, 0.1 mas translates to a projected distance of 0.51 pc. Additionally, the luminosity distance of S4 0954+65 is calculated to be 1980 Mpc.

These 43 GHz VLBA images of S4 0954+65 (Fig. 3) reveal the evolution of the compact region of the jet during three months, from 2023 April to the end of June. They show the motion of a prominent component (Q1) to the northwest of the compact core (C) along position angle $-42° \pm 7°$. This angle is calculated using the positions of the C and Q1 components (see Table 2); its uncertainty is derived using x and y positional uncertainties equivalent to 0.2 times the FWHM size of the components. This direction differs by $28° \pm 8°$ from the previously reported (prior to 2018; Weaver et al. 2022) jet direction, which was $\Psi_{jet,43} = -13.7° \pm 2.1°$. We have reconstructed the VLBA images of the source using a forward-modeling approach, implemented within the `eht-imaging` software package (Chael et al. 2016). This entails determining the best-fit solution of the geometrical model, compared with the visibility amplitudes, closure phases, and fractional polarization, in terms of the minimum of an error function (for further details see, e.g., Paraschos et al. 2024a,b). The modeling parameters for C and Q1 are summarized in Table 2.

At 43 GHz, the total flux of C dominates over that of Q1 by a factor of ∼7. In terms of compactness (as measured by the size of the radius of the FWHM total intensity), Q1 is initially comparable in size to C. Over the course of the next three months, Q1 expands from 0.07 to 0.09 mas FWHM. Q1 separated from C with a roughly constant proper motion of (0.80 ± 0.07) mas yr^{-1}, which translates to a projected apparent speed of $(18 \pm 2)\,c$ in the rest frame of the host galaxy. Assuming a constant, linear proper motion, we estimate that Q1 was ejected on MJD 59994 ± 4. The average polarization degree (Π) of C is 2.2%, while that of Q1 is 3.8%. We find that Π_{Q1} peaks at 6% on MJD 60096, near the time of the optical-X-ray flare. The polarization angle (Ψ) of C remains roughly aligned with that of Q1 on MJD 60036 and 60085 at 115° and 35°, respectively (i.e., $\Psi_{C,MJD60036} \parallel \Psi_{Q1,MJD60036} \sim 115°$ and $\Psi_{C,MJD60085} \parallel \Psi_{Q1,MJD60085} \sim 35°$). However, on MJD 60096 Ψ_C remains near its previous value, while Ψ_{Q1} rotates to 132° (i.e., $\Psi_{C,MJD60096} \perp \Psi_{Q1,MJD60096}$, roughly). The polarization degree and angle of C and Q1 are plotted as a function of time in Fig. 2.

4. Theoretical models

In this section, we describe the construction of the spectral energy distribution (SED) νF_ν (frequency multiplied by flux density at that frequency) and MWL spectral polarization distribution (SPD) of S4 0954+65, using only data obtained during the IXPE observation (MJD 60089-60098). The SPD represents how the polarization degree Π changes with respect to ν. Subsequently, we describe how we model these MWL spectral distributions based on two general scenarios: leptonic (single and multi-zone) and hadronic (proton + pair synchrotron).

To build the MWL SED and SPD, at each of our observed frequencies we determine the median and standard deviation of both the flux density and polarization degree. For the leptonic models, we use the single-zone (Böttcher et al. 2013) and

[7] https://fermi.gsfc.nasa.gov/ssc/data/access/lat/BackgroundModels.html

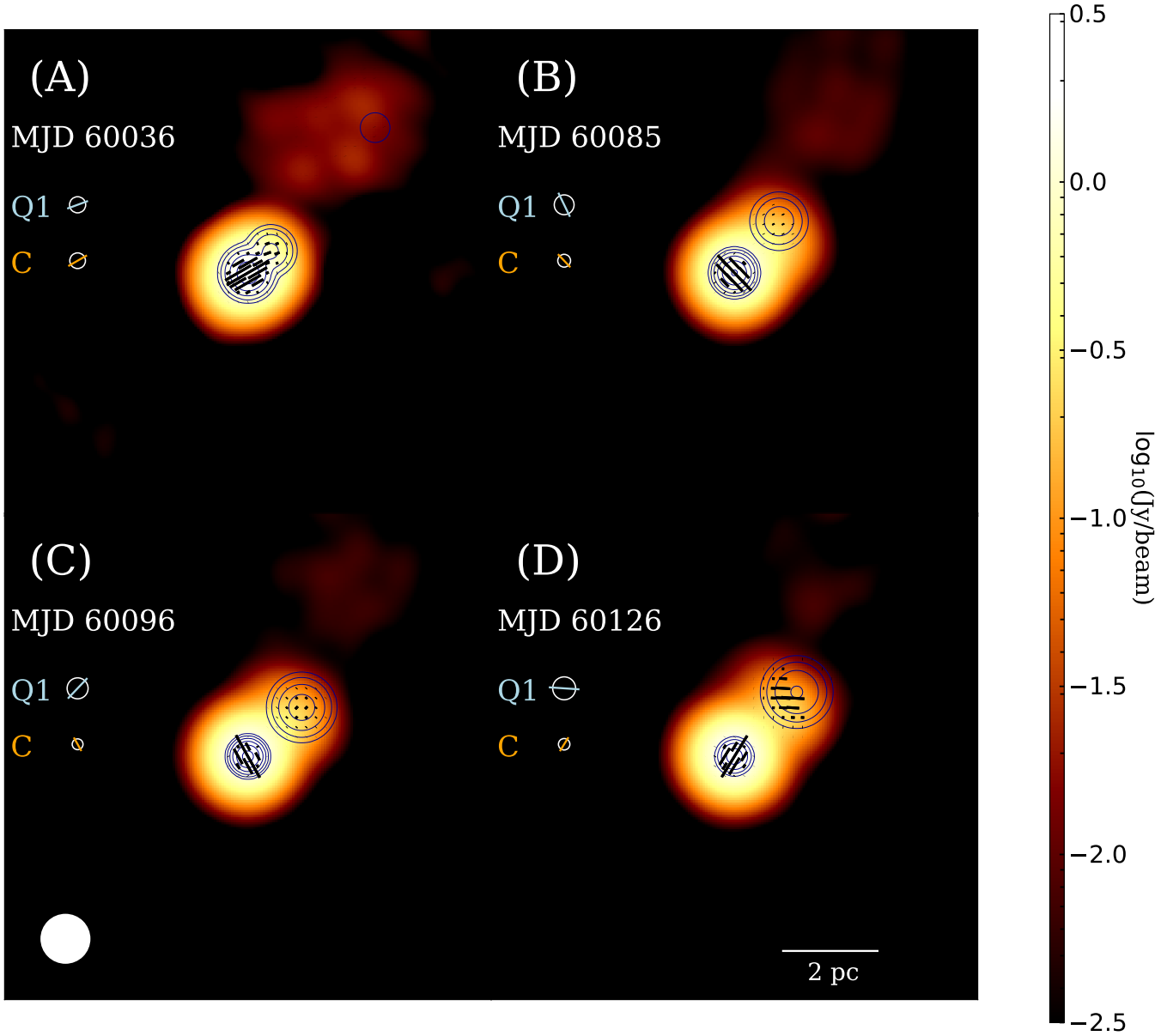

Fig. 3. 43 GHz total intensity (Stokes *I*) VLBA images of S4 0954+65. Panels (A), (B), (C), and (D) show the parsec-scale maps of the compact core of the source from data obtained on 2023 April 2 (MJD 60036; about two months before the IXPE observation), 2023 May 21 (MJD 60085; five days before the IXPE pointing), 2023 June 1 (MJD 60096; during the IXPE pointing and in the vicinity of the peak of the optical-X-ray flare), and 2023 July 1 (MJD 60126; around one month after the IXPE pointing), respectively. The bottom-left white circle is has a radius of 0.2 mas and is the FWHM of the common convolving beam. The circular contours are Stokes *I*, between 10^{-6} and 10^{-3} Jy in log steps. The general direction of the jet is consistently northwest ($-42° \pm 6°$). In panel (A), a component (Q1) north-northwest of the compact core (C) appears to separate from the core after being "ejected". The polarization angles of both C and Q1 are ∼115°. In panel (B), the polarization angles of both C and Q1 appear to have rotated to ∼35°. In panel (C), the polarization angle of C remains comparable to its value in (B), but that of Q1 has rotated by ∼100° compared to its value in (B). In panel (D), the polarization angle of C is 132°, while that of Q1 is 86°. In each panel, the angular size and polarization angle of the two components are represented by the circular symbols on the left (orange is used for the core component C and cyan is used for the moving component Q1): the radius of the circle symbolizes the angular size of each component (proportional to the FWHM of the intensity), while the orientation of the line through the circle visualizes the direction of the polarization angle.

multi-zone (Peirson & Romani 2019) SSC models. We find that we can adequately fit the high-energy portion of the SED without the need for an EC component, as is typical for BLLs and as was previously invoked for S4 0954+65 (e.g., Tanaka et al. 2016; see also Sect. 1). The multi-zone model accounts for depolarization and energy stratification but does not include synchrotron self-absorption effects. In this model, a conical jet with a fixed opening angle ($\theta_{\rm op}$) and constant Lorentz factor (Γ) is divided into magnetic field zones, each observed at a unique viewing angle ($\theta_{\rm obs}$), and thus has a Doppler factor $D = \frac{1}{\Gamma(1-\beta\cos\theta_{\rm obs})}$. The single-zone model uses the post-processing and semi-analytical depolarization procedure described in Zhang & Böttcher (2013) and Zhang et al. (2024), respectively. The hadronic model is post-processed with the same single-zone prescription[8] and mainly includes proton-synchrotron radiation. We note that the single-zone models (SSC and hadronic) do not fit the low-energy tail

[8] Given that the source was in a flaring state, the single-zone approximation for the hadronic emission is valid, even if the protons have an extended spatial distribution (Zhang et al. 2024).

Table 2. Component parameters of the 43 GHz VLBA maps shown in Fig. 3.

ID (1)	MJD (2)	F_0 (3)	R_I (4)	[x, y] (5)	Π (6)	Ψ (7)
C	60036	2.01	0.06	[0.00, 0.00]	2.2%	110°
C	60085	1.66	0.05	[0.00, 0.00]	3.4%	43°
C	60096	1.92	0.04	[0.00, 0.00]	3.0%	25°
C	60126	1.93	0.05	[0.00, 0.00]	0.3%	149°
Q1	60036	0.25	0.07	[−0.06, 0.07]	3.2%	120°
Q1	60085	0.27	0.08	[−0.14, 0.17]	1.8%	26°
Q1	60096	0.28	0.09	[−0.17, 0.19]	6.0%	132°
Q1	60126	0.28	0.09	[−0.20, 0.20]	4.2%	86°

Notes. Column (1) indicates the component ID (C refers to the core and Q1 refers to the component to the northwest of the core), column (2) gives the MJD of each map, column (3) gives the total flux density of the component in Jy, column (4) gives the radius of the full width at half maximum (FWHM) of the total intensity for each component in mas, column (5) gives the x and y coordinates of the components with respect to the core in mas, column (6) gives the polarization degree of the component in % (the typical errors on Π of C and Q1 are ±0.9% and ±0.6%, respectively), and column (7) gives the polarization angle of the component in degrees (the typical errors for Ψ are ±6°).

of the observed SED well, because in single-zone models emission from the large-scale jet is not included. Additionally, synchrotron self absorption is not taken into account when making the polarization calculations in any of the models. This limits our polarization estimates in the SPD to $\gtrsim 10^{12}$ Hz. Similarly, none of the polarization models includes Klein-Nishina effects; therefore, our Π calculations above $\sim 10^{24}$ Hz are not accurate.

Table 3 summarizes the SED modeling parameters for the different scenarios considered, while Fig. 4 presents the simultaneous SED and SPD modeling. For leptonic models, we find a drop of Π between the low- and high-energy components of the SED, as expected, whereas the hadronic model produces comparable polarization from optical to X-rays. More background information on the polarization behavior in leptonic versus hadronic scenarios is given in Sect. 1.

5. Discussion and conclusion

In this paper, we present the first X-ray polarization observation of the blazar S4 0954+65 in a flaring optical and X-ray state, which is the first X-ray polarization observation of a purely LSP blazar in outburst. All previous IXPE observations of purely LSP blazars were performed during quiescent states (Marshall et al. 2024) and those of the transitional LSP-ISP blazars, BL Lacertae and S5 0716+714, were either in an LSP-quiescent state or ISP-outburst state (Middei et al. 2023b; Peirson et al. 2023; Marshall et al. 2024).

Despite the X-ray flare, we are only able to place upper limits on the X-ray polarization degree, ($\Pi_X < 14\%$ at 99.73% confidence level, when considering the full, 2–8 keV, IXPE observation). We do not find any evidence for variability in either time or energy within the IXPE observing window. To obtain more constraining upper limits, we fix the X-ray polarization angle (Ψ_X) to values motivated by the direction of the jet on the sky or the optical polarization angle (Ψ_O). Table 1 summarizes the upper limits on the X-ray polarization degree in each of the scenarios. The most constraining upper limits we find are $\Pi_X < 8.4\%$ and $\Pi_X < 8.8\%$ (at 99.73% confidence levels), occurring when the X-ray polarization angle is assumed to be perpendicular to the constant optical polarization angle and the jet axis, respectively. However, since the optical and X-ray flares occurred in close proximity, the most likely scenario may be the latter (i.e., $\Psi_X \perp \Psi_{jet,43}$). This is because during the optical-X-ray flare Ψ_O was perpendicular to $\Psi_{jet,43}$, which implies that the magnetic field lines were parallel to the jet. For hadronic synchrotron emission originating from the same region, we would then expect $\Psi_X \perp \Psi_{jet,43}$. On the other hand, inferring a likely alignment for Ψ_X in the SSC scenarios is more complicated, as it depends on the orientation of the seed photon region, upscattering region, and line of sight; however, if we assume that all three are roughly aligned, then SSC would generally retain the direction of Ψ_O and yield $\Psi_X \perp \Psi_{jet,43}$. Nevertheless, we emphasize that without a significant detection of the polarization degree, any polarization angle inference should be treated with caution.

The simultaneous optical polarization observations show variations in both the polarization degree (Π_O) and angle (Ψ_O). Π_O varied stochastically about an average value of 14.3% with a standard deviation of 4.1%. The most extreme change in Π_O within the IXPE observation window occurred simultaneously with a ∼1 magnitude optical flare (from MJD 60092 to 60095), as Π_O increased from ∼6% to ∼20% (see Fig. 2). Intriguingly, exactly during this flaring period, Ψ_O remained stable at $66.5° \equiv -113.5°$, which is roughly perpendicular to the jet position angle ($\Psi_{jet,43} = -42 \pm 7$; see Sect. 3.3). Outside of this 3 d flaring time window, Ψ_O varied rapidly from approximately parallel to the jet axis to perpendicular and vice versa; even a daily $\Delta\Psi_O \sim 90°$ was detected (see Sect. 3). In Fig. 5 we present a rough timeline of how the MWL polarization angles of S4 0954+65 behaved.

Meanwhile, the radio polarization degree (Π_R) stayed consistently low (<4%; the average was 2.2% during the IXPE pointing with a standard deviation of 0.7%) and the radio polarization angles (Ψ_R), at the lower radio frequencies, were roughly perpendicular to $\Psi_{jet,43}$ during the entire IXPE pointing. On the 43 GHz parsec-scale VLBA images of S4 0954+65 (Fig. 3), we see a core component (C) and a second component (Q1) moving along the jet axis (i.e., northwest of the core) at an apparent superluminal motion of $18 \pm 2\,c$. The flux of C at 43 GHz dominates over Q1 by a factor of ∼7. Hence, the point-source polarization properties in the lower-frequency radio bands mainly probe the core. Indeed, when focusing on the VLBA maps obtained close to the IXPE pointing (MJD 60085 and 60096, panels B and C of Fig. 3, respectively), we find that the polarization properties of C ($\Pi_{R,C} \sim 3\%$ and $\Psi_{R,C} \sim 40°$, on average; see Table 2) match those of the single-dish observations at the lower-frequency radio bands. While the lack of variability in component C near the IXPE pointing is consistent with the single-dish radio observations, it fails to explain why the optical properties of S4 0954+65 varied so rapidly during our MWL time window. Instead, we can consider the moving component Q1 as a possible source of the optical flare. At MJD 60085, $\Psi_{R,Q1}$ was 25°, but it changed to 132° at MJD 60096. This behavior generally resembles that of Ψ_O around the same time (see Fig. 5). Additionally, $\Pi_{R,Q1}$ on MJD 60085 was 1.79%, which increased to 6.00% on MJD 60096. This tripling of the polarization degree of Q1 coincides with the increase in Π_O during the optical flare (from 6% to 20%). These similarities suggest that the observed optical variability and flare originated in the moving component Q1. This is consistent with previous observations of S4 0954+65 (Morozova et al. 2014; also see Sect. 1) and other blazars (e.g., Marscher et al. 2010), where optical variability has been associated with moving parsec-scale components.

Table 3. Parameters of the different SED models.

		SSC (multi-zone)	SSC (single-zone)	Hadronic
Bulk Lorentz factor	Γ	10	30	30
Bulk Doppler factor	D	–	30	30
Blob radius	R (cm)	2.4×10^{15}	7×10^{16}	10^{15}
Particle escaping time scale	$\tau_{\rm esc}$ (s)	–	10^{7}	10^{5}
Magnetic field strength	B (G)	0.12	0.028	100
Electron injection luminosity	L_e (erg/s)	–	2.6×10^{46}	1.3×10^{44}
Electron lower spectral cutoff	$\gamma_{e,\rm min}$	1	1	3×10^{2}
Electron higher spectral cutoff	$\gamma_{e,\rm max}$	1.2×10^{4}	2×10^{4}	10^{3}
Electron spectral index	p_e	1.7	2.2	2.37
Proton injection luminosity	L_p (erg/s)	–	–	3×10^{49}
Proton higher spectral cutoff	$\gamma_{p,\rm max}$	–	–	3×10^{8}
Proton spectral index	p_p	–	–	2.37
Jet Power	W_j (erg/s)	5×10^{45}	–	–
Opening angle	$\theta_{\rm open}$	8	–	–
Observing angle	$\theta_{\rm obs}$	1.5	–	–
Equilibrium factor	$A_{\rm eq}$	0.1	–	–
Number of zones	N	25	–	–

Notes. Column (1) is for the SSC multi-zone model at the base of the jet; column (2) for the single-zone SSC; and column (3) for the hadronic model. We note that the models are not fitted to the data, so that these model parameters are one representation of the data and not a unique solution.

Next, we examine the timing of the optical and X-ray flares. As described in Sect. 2.1 and visible in Fig. 1, the X-ray flux of S4 0954+65 measured by IXPE culminated between MJD 60094 and 60096 (peaking at MJD 60095). Meanwhile, there was a ∼1 magnitude optical flare which similarly peaked at MJD 60095. The lack of time delay between these flares implies that their emission regions are at least partially co-spatial. Since we have deduced that the optical flare most likely occurred in VLBA component Q1, it is likely that the X-ray flare also originated there.

Subsequently, we used the available data to constrain possible particle acceleration mechanisms within the moving component Q1, which likely caused the optical-X-ray flare. We began by considering the three commonly favored particle acceleration scenarios in blazar jets: shocks, magnetic reconnection, and turbulence. In diffusive shock acceleration, a shock front moving down the plasma jet energizes particles when they reflect back and forth across the front as they encounter magnetic irregularities (e.g., Blandford & Eichler 1987; Marscher & Gear 1985; Sikora et al. 1994). In magnetic reconnection scenarios, magnetic energy is efficiently converted into nonthermal particle energy at the interface between contiguous regions of parallel and antiparallel magnetic field lines (e.g., Guo et al. 2020; Zhang et al. 2020). These mechanisms can also occur in turbulent plasma either crossing a shock (e.g., Marscher 2014) or stochastically bringing together regions of opposite magnetic polarity, causing multiple reconnection events (e.g., Comisso & Sironi 2018; Zhang et al. 2023). In general, turbulence-based acceleration scenarios result in stochastic variations of the flux and polarization properties, especially at higher frequencies; this implies that their polarization angles can rotate with an arbitrary amplitude ($\Delta\Psi$), which tends to be greater when Π is near zero. The rotation is in a random direction (clockwise or counterclockwise), usually with no relation to flaring behavior. Notably, a similar stochastic behavior can also be expected from both shock-driven and magnetic reconnection acceleration scenarios, especially if the observed radiation originates from beyond their acceleration zone, where the environment may be more turbulent. However, they both can also result in non-stochastic changes in Π and Ψ, often in connection with flares, if the observed emission originates from less turbulent regions. In shocks, these changes are generally expected to be smoother, slower, and lower in amplitude compared to those that occur in magnetic reconnection (e.g., Di Gesu et al. 2022b).

In the case of S4 0954+65, whose synchrotron emission peaks in or near the optical band, $\Pi_{\rm O}$ appears to behave rather stochastically. This is in agreement with the turbulent element of all three aforementioned acceleration scenarios. However, it is difficult to ascertain whether the behavior of $\Psi_{\rm O}$ is completely stochastic, or has some ordered nature, owing to the rather short observation window of our MWL campaign. Nevertheless, it appears that $\Psi_{\rm O}$ preferentially stays parallel to the jet axis, while it rotates to be roughly perpendicular to the jet axis during the optical-X-ray flare, before returning back its original orientation. If this $\Psi_{\rm O}$ rotation is indeed caused by an ordered component of the magnetic field, we can disfavor stochastically driven acceleration scenarios. Additionally, even in a stochastic scenario, the rather high $\Pi_{\rm O}$ of ∼15–20% would imply a small number of emitting cells. These findings would support the shock-driven and magnetic reconnection scenarios, where the observed radiation comes from a partially ordered region.

In general, $\Psi_{\rm O}$ executes some rather long rotations ($\Delta\Psi_{\rm O}$ up to ∼90°), which favors magnetic reconnection over shocks. However, since we measure the combined polarization properties of all of the components of S4 0954+65, the rotations in $\Psi_{\rm O}$ could also be due to an interplay between its various polarized components (e.g., Cohen & Savolainen 2020). During a flare, this interplay is expected to have a weak effect, as the flaring component would be the sole dominant component. Notably, this is exactly what we have observed: during the optical-X-ray flare, $\Psi_{\rm O}$ remained nearly constant for three days. Such smooth and slow changes in $\Psi_{\rm O}$ during the flare suggests shocks. Furthermore, since $\Pi_{\rm O}/\Pi_{\rm R,Q1}$ was at least 2 during the optical-X-ray flare, the already well-established energy-stratified picture

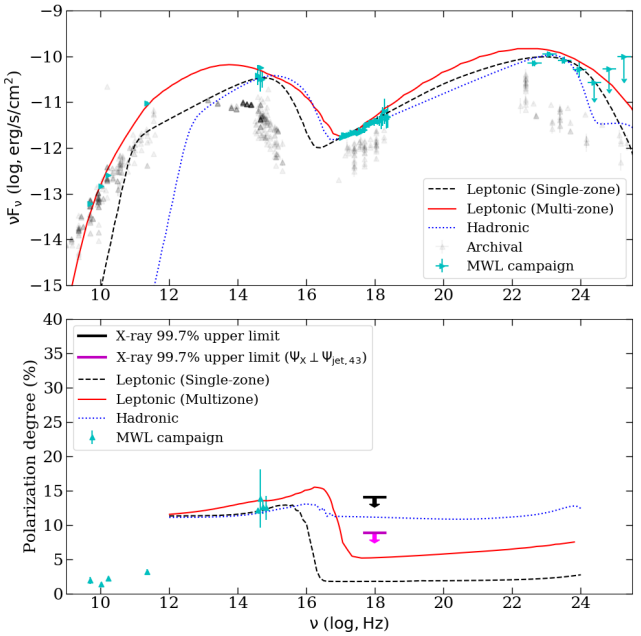

Fig. 4. Top: Spectral energy distribution (SED) of S4 0954+65. Bottom: Spectral polarization distribution (SPD) of S4 0954+65. In both panels, the cyan data points show the median and standard deviation values at different frequencies during the IXPE exposure. The archival observations (non-simultaneous) are shown in black for reference. The different models are represented by the solid, dashed, and dotted colored lines, as indicated in the legend. In the bottom panel the black downward arrow indicates the 3σ upper limit for the entire exposure, and the magenta arrow the 3σ upper limit under the assumption that the X-ray polarization angle is aligned perpendicular to the 43 GHz jet position angle (see Table 1).

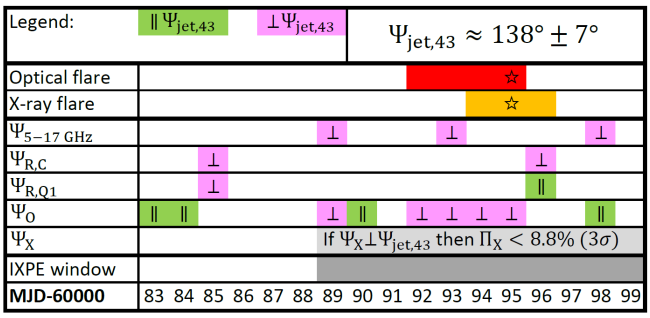

Fig. 5. Rough general timeline of the MWL observations of S4 0954+65.

(invoked when explaining the low-energy component of blazar emission; e.g., Liodakis et al. 2022b; Marscher et al. 2024; Kouch et al. 2024b) also applies in the case of S4 0954+65.

For most magnetic field geometries proposed for blazars, the polarization angle of the synchrotron emission of blazars (Ψ_O in the case of S4 0954+65) is expected to lie either parallel or perpendicular with respect to the jet position angle (e.g., Laing 1980; Lyutikov et al. 2005; Jorstad et al. 2007). In the case of BLLs, it is more often parallel to the jet axis (Hovatta et al. 2014). In shock fronts that compress the plasma along the jet, the magnetic field lines are expected to become more perpendicular to the jet axis. In addition, a helical magnetic field is more strongly toroidal than poloidal for most viewing angles; this results in polarization angles that are aligned with the axis of a relativistic jet (Lyutikov et al. 2005). On the other hand, when the longitudinal components of the ambient magnetic field are amplified by shearing of the internal jet flow or by interactions with the external medium, the magnetic field lines become more parallel to the jet axis. This shearing often happens close to the edge of jets (e.g., Laing 1980; Pushkarev et al. 2023). In such jets, while the passage of a shock would not amplify the ambient magnetic field, it would lead to more efficient particle acceleration in shocks that pass through the region. This would then result in a flare at higher frequencies, with polarization angles that are perpendicular to the jet axis (e.g., Marscher et al. 2002). This is precisely what we observe from S4 0954+65 during its optical-X-ray flare, which probably took place in its moving component Q1. We therefore propose that the flare occurs in Q1 as a moving shock (which creates Q1) propagates through a segment of the jet containing a magnetic field that is parallel to the jet axis. This accelerates particles, which then cool (leading to the optical-X-ray flare) in a region that has magnetic field lines aligned parallel to the jet axis. After the flare, the field encountered by the shock becomes more turbulent, such that the shock compresses the field to partially order it perpendicular to the jet axis. This causes the polarization angle to revert to a direction parallel to the jet axis. Nevertheless, we emphasize that this interpretation may not hold if there is any significant contribution to Π_O and Ψ_O from any other polarized components (e.g., C).

Regarding the high-energy component of blazar emission, as described in Sect. 1, Compton scattering (either EC and SSC) or hadronic processes could be operating. As seen from the SED (top panel in Fig. 4), all of the three models can adequately explain the observed data in the frequency ranges where they are relevant (see Sect. 4 for more details). Thus, to distinguish among them, we focus on the SPD (bottom panel in Fig. 4). It is apparent that all three of the models can adequately predict $\Pi_O \lesssim 14\%$. However, for the high-energy component (X-ray in the case of S4 0954+65), the SSC models predict $\Pi_X < \Pi_O$, while the hadronic model predicts $\Pi_X \sim \Pi_O$. As shown in Table 1, we obtain $\Pi_X < 14\%$ and $\Pi_X < 8.8\%$ (at 99.73% confidence levels) when no assumption about Ψ_X is made and when the most likely alignment scenario (i.e., $\Psi_X \perp \Psi_{jet,43}$; see above for justification) is assumed, respectively. While these upper limits do not allow us to definitively distinguish between leptonic and hadronic scenarios, they strongly disfavor purely hadronic scenarios. This is consistent with all of the previous IXPE observations of LSP and ISP sources (Middei et al. 2023b; Marshall et al. 2024; Peirson et al. 2023). Another argument against a purely hadronic scenario for S4 0954+65 comes directly from the aforementioned conclusion that the optical and X-ray emission regions are roughly co-spatial during the flare. This conflicts with a hadronic scenario, since protons are expected to be distributed over a more extended region than electrons (Zhang et al. 2024) and protons need much stronger magnetic fields than electrons for efficient synchrotron cooling (Liodakis & Petropoulou 2020). Furthermore, a variability timescale analysis based on electron synchrotron cooling time in the observer frame $\tau_{var} = 1200\, B^{-1.5} E^{-0.5} D^{-0.5} (1+z)$, where τ_{var} is in seconds, B is the strength of the comoving magnetic field in G, E is the photon energy in keV, D is the Doppler factor, and z is the redshift (e.g., Cristiani et al. 1996; Baloković et al. 2016), reveals $\tau_{var} \sim 13$ days for the single-zone SSC model ($B = 0.028$ G and $D = 30$; see Table 3) in the optical band ($E = 3$ eV), which is of the same order as the observed flaring timescale of ~5 days. On the other hand, in the hadronic model ($B = 100$ G and $D = 30$), the proton synchrotron cooling

timescale[9] in the observer frame is ∼26 years in the IXPE band ($E = 5$ keV). While faster variability in the hadronic model may still arise due to more rapid plasma dynamical timescales, the observed variability timescale is more difficult to accommodate under the hadronic scenario. As a result, we ultimately favor leptonic models over hadronic ones to explain the origin of the X-ray emission of S4 0954+65 and the emission of the high-energy component of blazars as a whole; however, without a significant detection of Π_X, alternative interpretations remain possible.

In the case of S4 0954+65, since the emitting region of the optical-X-ray flare is most likely in the Q1 component (i.e., on the order of parsecs from the core where the likely sources of EC seed photons are found), SSC is more likely than EC. Furthermore, when modeling the SED of S4 0954+65 (see Sect. 4), we found that SSC alone can fit the observed behavior quite well, without the need for a contribution from EC.

To set more definitive constraints on the high-energy emission models of supermassive black hole jets, we need more observations of LSP blazars when they are in a brighter X-ray flux state or highly polarized in the optical band. Additionally, detailed modeling of the radio and optical polarization variability, as well as that of the radio morphology would be very helpful to further constrain the jet dynamics and put stronger constraints on the polarization degree under a hadronic model. BLLs, such as S4 0954+65, whose SEDs can be adequately described by SSC without the need for an EC component offer an additional advantage, as their SED modeling is rather straightforward. Furthermore, Π_O of S4 0954+65 often exceeds >25% (Raiteri et al. 2023; Liodakis et al. 2023), which makes it a prime target for future campaigns with IXPE and future higher-energy polarimeters (e.g., COSI; Tomsick et al. 2023).

Acknowledgements. We thank the anonymous referee for constructive suggestions that helped improve and clarify the paper. The Imaging X-ray Polarimetry Explorer (IXPE) is a joint US and Italian mission. The US contribution is supported by the National Aeronautics and Space Administration (NASA) and led and managed by its Marshall Space Flight Center (MSFC), with industry partner Ball Aerospace (now, BAE Systems). The Italian contribution is supported by the Italian Space Agency (Agenzia Spaziale Italiana, ASI) through contract ASI-OHBI-2022-13-I.0, agreements ASI-INAF-2022-19-HH.0 and ASI-INFN-2017.13-H0, and its Space Science Data Center (SSDC) with agreements ASI-INAF-2022-14-HH.0 and ASI-INFN 2021-43-HH.0, and by the Istituto Nazionale di Astrofisica (INAF) and the Istituto Nazionale di Fisica Nucleare (INFN) in Italy. This research used data products provided by the IXPE Team (MSFC, SSDC, INAF, and INFN) and distributed with additional software tools by the High-Energy Astrophysics Science Archive Research Center (HEASARC), at NASA Goddard Space Flight Center (GSFC). This work has been partially supported by the ASI-INAF program I/004/11/4. The IAA-CSIC co-authors acknowledge financial support from the Spanish "Ministerio de Ciencia e Innovación" (MCIN/AEI/10.13039/501100011033) through the Center of Excellence Severo Ochoa award for the Instituto de Astrofíisica de Andalucía-CSIC (CEX2021-001131-S), and through grants PID2019-107847RB-C44 and PID2022-139117NB-C44. The Submillimeter Array is a joint project between the Smithsonian Astrophysical Observatory and the Academia Sinica Institute of Astronomy and Astrophysics and is funded by the Smithsonian Institution and the Academia Sinica. Maunakea, the location of the SMA, is a culturally important site for the indigenous Hawai'ian people; we are privileged to study the cosmos from its summit. E.L. was supported by Academy of Finland projects 317636 and 320045. D.B. acknowledges support from the European Research Council (ERC) under the Horizon ERC Grants 2021 programme under the grant agreement No. 101040021. The research at Boston University was supported in part by National Science Foundation grant AST-2108622, NASA Fermi Guest Investigator grants 80NSSC23K1507 and 80NSSC23K1508, and NASA *Swift* Guest Investigator grant 80NSSC23K1145. The Perkins Telescope Observatory, located in Flagstaff, AZ, USA, is owned and operated by Boston University. IL and SK were funded by the European Union ERC-2022-STG – BOOTES – 101076343. Views and opinions expressed are however those of the author(s) only and do not necessarily reflect those of the European Union or the European Research Council Executive Agency. Neither the European Union nor the granting authority can be held responsible for them. Some of the data are based on observations collected at the Centro Astronómico Hispano en Andalucía (CAHA), operated jointly by Junta de Andalucía and Consejo Superior de Investigaciones Científicas (IAA-CSIC). This work was supported by NSF grant AST-2109127. We acknowledge the use of public data from the *Swift* data archive. Based on observations obtained with *XMM-Newton*, an ESA science mission with instruments and contributions directly funded by ESA Member States and NASA. Partly based on observations with the 100-m telescope of the MPIfR (Max-Planck-Institut für Radioastronomie) at Effelsberg. Observations with the 100-m radio telescope at Effelsberg have received funding from the European Union's Horizon 2020 research and innovation programme under grant agreement No 101004719 (ORP). I.L. was supported by the NASA Postdoctoral Program at the Marshall Space Flight Center, administered by Oak Ridge Associated Universities under contract with NASA. HZ is supported by NASA under award number 80GSFC21M0002. HZ's work is supported by Fermi GI program cycle 16 under the award number 22-FERMI22-0015. G.F.P. acknowledges support by the European Research Council advanced grant "M2FINDERS – Mapping Magnetic Fields with INterferometry Down to Event hoRizon Scales" (Grant No. 101018682). S. Kang, S.-S. Lee, W. Y. Cheong, S.-H. Kim, and H.-W. Jeong were supported by the National Research Foundation of Korea (NRF) grant funded by the Korea government (MIST) (2020R1A2C2009003). The KVN is a facility operated by the Korea Astronomy and Space Science Institute. The KVN operations are supported by KREONET (Korea Research Environment Open NETwork) which is managed and operated by KISTI (Korea Institute of Science and Technology Information). This work was supported by JST, the establishment of university fellowships towards the creation of science technology innovation, Grant Number JPMJFS2129. This work was supported by Japan Society for the Promotion of Science (JSPS) KAKENHI Grant Numbers JP21H01137. This work was also partially supported by Optical and Near-Infrared Astronomy Inter-University Cooperation Program from the Ministry of Education, Culture, Sports, Science and Technology (MEXT) of Japan. We are grateful to the observation and operating members of Kanata Telescope. Data from the Steward Observatory spectropolarimetric monitoring project were used. This program is supported by Fermi Guest Investigator grants NNX08AW56G, NNX09AU10G, NNX12AO93G, and NNX15AU81G. This research was partially supported by the Bulgarian National Science Fund of the Ministry of Education and Science under grants KP-06-H38/4 (2019) and KP-06-PN-68/1 (2022). The Liverpool Telescope is operated on the island of La Palma by Liverpool John Moores University in the Spanish Observatorio del Roque de los Muchachos of the Instituto de Astrofisica de Canarias with financial support from the UKRI Science and Technology Facilities Council (STFC) (ST/T00147X/1). This study makes use of VLBA data from the VLBA-BU Blazar Monitoring Program (BEAM-ME and VLBA-BU-BLAZAR; http://www.bu.edu/blazars/BEAM-ME.html), funded by NASA through the Fermi Guest Investigator Program. The VLBA is an instrument of the National Radio Astronomy Observatory. The National Radio Astronomy Observatory is a facility of the National Science Foundation operated by Associated Universities, Inc. Based on observations obtained with the Samuel Oschin Telescope 48-inch and the 60-inch Telescope at the Palomar Observatory as part of the Zwicky Transient Facility project. ZTF is supported by the National Science Foundation under Grant No. AST-2034437 and a collaboration including Caltech, IPAC, the Weizmann Institute for Science, the Oskar Klein Center at Stockholm University, the University of Maryland, Deutsches Elektronen-Synchrotron and Humboldt University, the TANGO Consortium of Taiwan, the University of Wisconsin at Milwaukee, Trinity College Dublin, Lawrence Livermore National Laboratories, and IN2P3, France. Operations are conducted by COO, IPAC, and UW. The ZTF forced-photometry service was funded under the Heising-Simons Foundation grant #12540303 (PI: M.J.Graham). This work has made use of data from the Asteroid Terrestrial-impact Last Alert System (ATLAS) project. The Asteroid Terrestrial-impact Last Alert System (ATLAS) project is primarily funded to search for near earth asteroids through NASA grants NN12AR55G, 80NSSC18K0284, and 80NSSC18K1575; byproducts of the NEO search include images and catalogs from the survey area. This work was partially funded by Kepler/K2 grant J1944/80NSSC19K0112 and HST GO-15889, and STFC grants ST/T000198/1 and ST/S006109/1. The ATLAS science products have been made possible through the contributions of the University of Hawai'i Institute for Astronomy, the Queen's University Belfast, the Space Telescope Science Institute, the South African Astronomical Observatory, and The Millennium Institute of Astrophysics (MAS), Chile. This publication makes use of the Metsähovi Radio Observatory facilities, operated by the Aalto University, Finland. We thank Talvikki Hovatta and Tuomas Savolainen for fruitful discussions.

[9] The proton cooling timescale is longer by a factor of $(m_p/m_e)^3 \approx 6 \times 10^9$ than the electron cooling timescale (e.g., Begelman et al. 1990).

References

Abdo, A. A., Ackermann, M., Ajello, M., et al. 2010, ApJ, 710, 1271

Abdollahi, S., Acero, F., Ackermann, M., et al. 2020, ApJS, 247, 33
Bachev, R. 2015, MNRAS, 451, L21
Baldini, L., Bucciantini, N., Lalla, N. D., et al. 2022, SoftwareX, 19, 101194
Ballet, J., Burnett, T. H., Digel, S. W., & Lott, B. 2020, arXiv e-prints [arXiv:2005.11208]
Baloković, M., Paneque, D., Madejski, G., et al. 2016, ApJ, 819, 156
Becerra González, J., Acosta-Pulido, J. A., Boschin, W., et al. 2021, MNRAS, 504, 5258
Begelman, M. C., & Sikora, M. 1987, ApJ, 322, 650
Begelman, M. C., Rudak, B., & Sikora, M. 1990, ApJ, 362, 38
Bellm, E. C., Kulkarni, S. R., Graham, M. J., et al. 2019, PASP, 131, 018002
Blandford, R., & Eichler, D. 1987, Phys. Rep., 154, 1
Blandford, R., Meier, D., & Readhead, A. 2019, ARA&A, 57, 467
Boettcher, M., Fu, M., Govenor, T., King, Q., & Roustazadeh, P. 2022, arXiv e-prints [arXiv:2204.12242]
Bonometto, S., & Saggion, A. 1973, A&A, 23, 9
Bonometto, S., Cazzola, P., & Saggion, A. 1970, A&A, 7, 292
Böttcher, M. 2019, Galaxies, 7, 20
Böttcher, M., Reimer, A., Sweeney, K., & Prakash, A. 2013, ApJ, 768, 54
Cash, W. 1979, ApJ, 228, 939
Chael, A. A., Johnson, M. D., Narayan, R., et al. 2016, ApJ, 829, 11
Chen, C.-T. J., Liodakis, I., Middei, R., et al. 2024, ApJ, 974, 50
Cohen, M. H., & Savolainen, T. 2020, A&A, 636, A79
Comisso, L., & Sironi, L. 2018, Phys. Rev. Lett., 121, 255101
Cristiani, S., Trentini, S., La Franca, F., et al. 1996, A&A, 306, 395
Deng, J. H., Hu, S. M., Jiang, Z. J., Xiang, Y. C., & Zhou, R. X. 2022, Ap&SS, 367, 43
Dermer, C. D., Schlickeiser, R., & Mastichiadis, A. 1992, A&A, 256, L27
Dickey, J. M., & Lockman, F. J. 1990, ARA&A, 28, 215
Di Gesu, L., Donnarumma, I., Tavecchio, F., et al. 2022a, ApJ, 938, L7
Di Gesu, L., Tavecchio, F., Donnarumma, I., et al. 2022b, A&A, 662, A83
Di Gesu, L., Marshall, H. L., Ehlert, S. R., et al. 2023, Nat. Astron., 7, 1245
Di Marco, A., Costa, E., Muleri, F., et al. 2022, AJ, 163, 170
Di Marco, A., Soffitta, P., Costa, E., et al. 2023, AJ, 165, 143
Ehlert, S. R., Ferrazzoli, R., Marinucci, A., et al. 2022, ApJ, 935, 116
Ehlert, S. R., Liodakis, I., Middei, R., et al. 2023, ApJ, 959, 61
Errando, M., Liodakis, I., Marscher, A. P., et al. 2024, ApJ, 963, 5
Gabuzda, D. C., Kochenov, P. Y., Kollgaard, R. I., & Cawthorne, T. V. 2000, MNRAS, 315, 229
Gehrels, N., Chincarini, G., Giommi, P., et al. 2004, ApJ, 611, 1005
Ghisellini, G., Tavecchio, F., Foschini, L., & Ghirlanda, G. 2011, MNRAS, 414, 2674
Guo, F., Liu, Y.-H., Li, X., et al. 2020, Phys. Plasmas, 27, 080501
HI4PI Collaboration (Ben Bekhti, N., et al.) 2016, A&A, 594, A116
Ho, P. T. P., Moran, J. M., & Lo, K. Y. 2004, ApJ, 616, L1
Hovatta, T., & Lindfors, E. 2019, New Astron. Rev., 87, 101541
Hovatta, T., Aller, M. F., Aller, H. D., et al. 2014, AJ, 147, 143
Hovatta, T., Lindfors, E., Blinov, D., et al. 2016, A&A, 596, A78
IceCube Collaboration (Aartsen, M. G., et al.) 2018, Science, 361, eaat1378
Jansen, F., Lumb, D., Altieri, B., et al. 2001, A&A, 365, L1
Jones, T. W., O'Dell, S. L., & Stein, W. A. 1974, ApJ, 188, 353
Jorstad, S., & Marscher, A. 2016, Galaxies, 4, 47
Jorstad, S. G., Marscher, A. P., Stevens, J. A., et al. 2007, AJ, 134, 799
Jorstad, S. G., Marscher, A. P., Morozova, D. A., et al. 2017, ApJ, 846, 98
Kaastra, J. S. 2017, A&A, 605, A51
Kim, D. E., Di Gesu, L., Liodakis, I., et al. 2024, A&A, 681, A12
Kislat, F., Clark, B., Beilicke, M., & Krawczynski, H. 2015, Astropart. Phys., 68, 45
Kouch, P. M., Lindfors, E., Hovatta, T., et al. 2024a, A&A, 690, A111
Kouch, P. M., Liodakis, I., Middei, R., et al. 2024b, A&A, 689, A119
Krauss, F. 2014, ATel, 6709, 1
Kraus, A., Krichbaum, T. P., Wegner, R., et al. 2003, A&A, 401, 161
Krawczynski, H. 2012, ApJ, 744, 30
Laing, R. A. 1980, MNRAS, 193, 439
Lawrence, A., Walker, D., Rowan-Robinson, M., Leech, K. J., & Penston, M. V. 1986, MNRAS, 219, 687
Liodakis, I., & Petropoulou, M. 2020, ApJ, 893, L20
Liodakis, I., Peirson, A. L., & Romani, R. W. 2019, ApJ, 880, 29
Liodakis, I., Blinov, D., Potter, S. B., & Rieger, F. M. 2022a, MNRAS, 509, L21
Liodakis, I., Marscher, A. P., Agudo, I., et al. 2022b, Nature, 611, 677
Liodakis, I., Shablovinskaya, E., Blinov, D., et al. 2023, A&A, 680, L11
Lister, M. L., Aller, M. F., Aller, H. D., et al. 2018, ApJS, 234, 12
Lyutikov, M., Pariev, V. I., & Gabuzda, D. C. 2005, MNRAS, 360, 869
MAGIC Collaboration (Ahnen, M. L., et al.) 2018, A&A, 617, A30
Mannheim, K., & Biermann, P. L. 1989, A&A, 221, 211
Maraschi, L., Ghisellini, G., & Celotti, A. 1992, ApJ, 397, L5
Marchili, N., Krichbaum, T. P., Liu, X., et al. 2012, A&A, 542, A121
Marrone, D. P., & Rao, R. 2008, in Millimeter and Submillimeter Detectors and Instrumentation for Astronomy IV, eds. W. D. Duncan, W. S. Holland, S. Withington, & J. Zmuidzinas, Society of Photo-Optical Instrumentation Engineers (SPIE) Conference Series, 7020, 70202B
Marscher, A. P. 2014, ApJ, 780, 87
Marscher, A. P., & Gear, W. K. 1985, ApJ, 298, 114
Marscher, A. P., Jorstad, S. G., Mattox, J. R., & Wehrle, A. E. 2002, ApJ, 577, 85
Marscher, A. P., Jorstad, S. G., D'Arcangelo, F. D., et al. 2008, Nature, 452, 966
Marscher, A. P., Jorstad, S. G., Larionov, V. M., et al. 2010, ApJ, 710, L126
Marscher, A. P., Di Gesu, L., Jorstad, S. G., et al. 2024, Galaxies, 12, 50
Marshall, H. L., Liodakis, I., Marscher, A. P., et al. 2024, ApJ, 972, 74
Mead, A. R. G., Ballard, K. R., Brand, P. W. J. L., et al. 1990, A&AS, 83, 183
Middei, R., Perri, M., Puccetti, S., et al. 2023a, ApJ, 953, L28
Middei, R., Liodakis, I., Perri, M., et al. 2023b, ApJ, 942, L10
Morozova, D. A., Larionov, V. M., Troitsky, I. S., et al. 2014, AJ, 148, 42
Mukherjee, R., Aller, H. D., Aller, M. F., et al. 1995, ApJ, 445, 189
Myserlis, I. 2024, https://doi.org/10.5281/zenodo.14021047
Myserlis, I., Angelakis, E., Kraus, A., et al. 2018, A&A, 609, A68
Nilsson, K., Lindfors, E., Takalo, L. O., et al. 2018, A&A, 620, A185
Padovani, P., Resconi, E., Giommi, P., Arsioli, B., & Chang, Y. L. 2016, MNRAS, 457, 3582
Pandey, A., Bachev, R., Czerny, B., et al. 2023, A&A, 679, A28
Paraschos, G. F., Kim, J. Y., Wielgus, M., et al. 2024a, A&A, 682, L3
Paraschos, G. F., Wielgus, M., Benke, P., et al. 2024b, A&A, 687, L6
Peirson, A. L., & Romani, R. W. 2019, ApJ, 885, 76
Peirson, A. L., Negro, M., Liodakis, I., et al. 2023, ApJ, 948, L25
Petropoulou, M., Murase, K., Santander, M., et al. 2020, ApJ, 891, 115
Piconcelli, E., Jimenez-Bailón, E., Guainazzi, M., et al. 2004, MNRAS, 351, 161
Poutanen, J. 1994, ApJS, 92, 607
Pushkarev, A. B., Aller, H. D., Aller, M. F., et al. 2023, MNRAS, 520, 6053
Raiteri, C. M., Villata, M., Tosti, G., et al. 1999, A&A, 352, 19
Raiteri, C. M., Villata, M., Larionov, V. M., et al. 2021, MNRAS, 504, 5629
Raiteri, C. M., Villata, M., Carnerero, M. I., et al. 2023, MNRAS, 526, 4502
Ramaprakash, A. N., Rajarshi, C. V., Das, H. K., et al. 2019, MNRAS, 485, 2355
Sharma, A., Kamaram, S. R., Prince, R., Khatoon, R., & Bose, D. 2024, MNRAS, 527, 2672
Sikora, M., Begelman, M. C., & Rees, M. J. 1994, ApJ, 421, 153
Strüder, L., Briel, U., Dennerl, K., et al. 2001, A&A, 365, L18
Tanaka, Y. T., Becerra Gonzalez, J., Itoh, R., et al. 2016, PASJ, 68, 51
Tomsick, J. A., Boggs, S. E., Zoglauer, A., et al. 2023, arXiv e-prints [arXiv:2308.12362]
Tonry, J. L., Denneau, L., Heinze, A. N., et al. 2018, PASP, 130, 064505
Ulrich, M.-H., Maraschi, L., & Urry, C. M. 1997, ARA&A, 35, 445
Verner, D. A., Ferland, G. J., Korista, K. T., & Yakovlev, D. G. 1996, ApJ, 465, 487
Weaver, Z. R., Jorstad, S. G., Marscher, A. P., et al. 2022, ApJS, 260, 12
Weisskopf, M. C., Soffitta, P., Baldini, L., et al. 2022, J. Astron. Telesc. Instrum. Syst., 8, 026002
Wilms, J., Allen, A., & McCray, R. 2000, ApJ, 542, 914
Zhang, H., & Böttcher, M. 2013, ApJ, 774, 18
Zhang, H., Diltz, C., & Böttcher, M. 2016, ApJ, 829, 69
Zhang, H., Fang, K., Li, H., et al. 2019, ApJ, 876, 109
Zhang, H., Li, X., Giannios, D., et al. 2020, ApJ, 901, 149
Zhang, H., Marscher, A. P., Guo, F., et al. 2023, ApJ, 949, 71
Zhang, H., Böttcher, M., & Liodakis, I. 2024, ApJ, 967, 93

[1] Department of Physics and Astronomy, University of Turku, FI-20014 Turku, Finland
[2] Finnish Centre for Astronomy with ESO (FINCA), Quantum, Vesilinnantie 5, University of Turku, FI-20014 Turku, Finland
[3] Institute of Astrophysics, FORTH, N. Plastira 100, GR-70013 Heraklion, Greece
[4] NASA Marshall Space Flight Center, Huntsville, AL 35812, USA
[5] ASI – Agenzia Spaziale Italiana, Via del Politecnico snc, 00133 Roma, Italy
[6] University of Maryland, Baltimore County, Baltimore, MD 21250, USA
[7] NASA Goddard Space Flight Center, Greenbelt, MD 20771, USA
[8] INAF Osservatorio Astronomico di Brera, Via E. Bianchi 46, 23807 Merate (LC), Italy
[9] Space Science Data Center, Agenzia Spaziale Italiana, Via del Politecnico snc, 00133 Roma, Italy
[10] INAF Osservatorio Astronomico di Roma, Via Frascati 33, 00078 Monte Porzio Catone (RM), Italy

[11] Max-Planck-Institut für Radioastronomie, Auf dem Hügel 69, D-53121 Bonn, Germany
[12] Instituto de Astrofísica de Andalucía, IAA-CSIC, Glorieta de la Astronomía s/n, 18008 Granada, Spain
[13] Institute for Astrophysical Research, Boston University, 725 Commonwealth Avenue, Boston, MA 02215, USA
[14] Saint Petersburg State University, 7/9 Universitetskaya nab., St. Petersburg 199034, Russia
[15] Physics Department and McDonnell Center for the Space Sciences, Washington University in St. Louis, St. Louis, MO 63130, USA
[16] Department of Physics and Astronomy, Louisiana State University, Baton Rouge, LA 70803, USA
[17] INAF Istituto di Astrofisica e Planetologia Spaziali, Via del Fosso del Cavaliere 100, 00133 Roma, Italy
[18] Dipartimento di Fisica, Università degli Studi di Roma "La Sapienza", Piazzale Aldo Moro 5, 00185 Roma, Italy
[19] Dipartimento di Fisica, Università degli Studi di Roma "Tor Vergata", Via della Ricerca Scientifica 1, 00133 Roma, Italy
[20] Department of Physics, University of Crete, 70013 Heraklion, Greece
[21] Department of Mathematics and Applied Mathematics – Applied Mathematics, University of Crete, 70013 Heraklion, Greece
[22] Crimean Astrophysical Observatory RAS, P/O Nauchny 298409, Crimea
[23] Pulkovo Observatory, St. Petersburg 196140, Russia
[24] Geological and Mining Institute of Spain (IGME-CSIC), Calle Ríos Rosas 23, E-28003 Madrid, Spain
[25] Institut de Radioastronomie Millimétrique, Avenida Divina Pastora, 7, Local 20, E-18012 Granada, Spain
[26] Center for Astrophysics | Harvard & Smithsonian, 60 Garden St, Cambridge, MA 02138, USA
[27] Orchideenweg 8, D-53123 Bonn, Germany
[28] INAF Osservatorio Astronomico di Cagliari, Via della Scienza 5, 09047 Selargius (CA), Italy
[29] Istituto Nazionale di Fisica Nucleare, Sezione di Pisa, Largo B. Pontecorvo 3, 56127 Pisa, Italy
[30] Dipartimento di Fisica, Università di Pisa, Largo B. Pontecorvo 3, 56127 Pisa, Italy
[31] Naval Research Laboratory, 4555 Overlook Ave. SW, Washington, DC 20375, USA
[32] Dipartimento di Matematica e Fisica, Università degli Studi Roma Tre, Via della Vasca Navale 84, 00146 Roma, Italy
[33] Istituto Nazionale di Fisica Nucleare, Sezione di Torino, Via Pietro Giuria 1, 10125 Torino, Italy
[34] Dipartimento di Fisica, Università degli Studi di Torino, Via Pietro Giuria 1, 10125 Torino, Italy
[35] INAF Osservatorio Astrofisico di Arcetri, Largo Enrico Fermi 5, 50125 Firenze, Italy
[36] Dipartimento di Fisica e Astronomia, Università degli Studi di Firenze, Via Sansone 1, 50019 Sesto Fiorentino (FI), Italy
[37] Istituto Nazionale di Fisica Nucleare, Sezione di Firenze, Via Sansone 1, 50019 Sesto Fiorentino (FI), Italy
[38] Science and Technology Institute, Universities Space Research Association, Huntsville, AL 35805, USA
[39] Istituto Nazionale di Fisica Nucleare, Sezione di Roma "Tor Vergata", Via della Ricerca Scientifica 1, 00133 Roma, Italy
[40] Department of Physics and Kavli Institute for Particle Astrophysics and Cosmology, Stanford University, Stanford, California 94305, USA
[41] Institut für Astronomie und Astrophysik, Universität Tübingen, Sand 1, 72076 Tübingen, Germany
[42] Astronomical Institute of the Czech Academy of Sciences, Boční II 1401/1, 14100 Praha 4, Czech Republic
[43] RIKEN Cluster for Pioneering Research, 2-1 Hirosawa, Wako, Saitama 351-0198, Japan
[44] Yamagata University, 1-4-12 Kojirakawa-machi, Yamagata-shi 990-8560, Japan
[45] Osaka University, 1-1 Yamadaoka, Suita, Osaka 565-0871, Japan
[46] University of British Columbia, Vancouver BC V6T 1Z4, Canada
[47] International Center for Hadron Astrophysics, Chiba University, Chiba 263-8522, Japan
[48] Department of Physics and Astronomy and Space Science Center, University of New Hampshire, Durham, NH 03824, USA
[49] Istituto Nazionale di Fisica Nucleare, Sezione di Napoli, Strada Comunale Cinthia, 80126 Napoli, Italy
[50] Université de Strasbourg, CNRS, Observatoire Astronomique de Strasbourg, UMR 7550, 67000 Strasbourg, France
[51] MIT Kavli Institute for Astrophysics and Space Research, Massachusetts Institute of Technology, 77 Massachusetts Avenue, Cambridge, MA 02139, USA
[52] Graduate School of Science, Division of Particle and Astrophysical Science, Nagoya University, Furo-cho, Chikusa-ku, Nagoya, Aichi 464-8602, Japan
[53] Hiroshima Astrophysical Science Center, Hiroshima University, 1-3-1 Kagamiyama, Higashi-Hiroshima, Hiroshima 739-8526, Japan
[54] Department of Physics, The University of Hong Kong, Pokfulam, Hong Kong
[55] Department of Astronomy and Astrophysics, Pennsylvania State University, University Park, PA 16802, USA
[56] Université Grenoble Alpes, CNRS, IPAG, 38000 Grenoble, France
[57] Dipartimento di Fisica e Astronomia, Università degli Studi di Padova, Via Marzolo 8, 35131 Padova, Italy
[58] Department of Astronomy, University of Maryland, College Park, Maryland 20742, USA
[59] Mullard Space Science Laboratory, University College London, Holmbury St Mary, Dorking, Surrey RH5 6NT, UK
[60] Anton Pannekoek Institute for Astronomy & GRAPPA, University of Amsterdam, Science Park 904, 1098 XH Amsterdam, The Netherlands
[61] Guangxi Key Laboratory for Relativistic Astrophysics, School of Physical Science and Technology, Guangxi University, Nanning 530004, China

Appendix A: *Swift*-XRT and *XMM-Newton* data

In Table A.1, we tabulate the best-fit *Swift*-XRT and *XMM-Newton* results.

Table A.1. Best-fit *Swift*-XRT and *XMM-Newton* results when individually fitting the spectra.

Instrument	Obs. ID	MJD	t_{exp}	Photon index	Flux	C-statistics	Theoretical C-statistics
Swift-XRT	00015977001	60050.2	1.573	$1.33^{+0.11}_{-0.11}$	$8.8^{+0.9}_{-0.9}$	106.04	186.43 ± 16.07
	00015977002	60053.0	1.801	$1.34^{+0.11}_{-0.13}$	$7.0^{+1.0}_{-0.7}$	124.63	153.38 ± 14.53
	00015977003	60060.0	1.281	$1.31^{+0.10}_{-0.10}$	$13.7^{+1.3}_{-1.2}$	178.81	205.77 ± 17.51
	00097199001	60087.0	0.931	$1.58^{+0.15}_{-0.14}$	$7.6^{+1.0}_{-0.9}$	113.87	112.41 ± 12.23
	00097199002	60088.0	0.862	$1.55^{+0.15}_{-0.17}$	$6.7^{+1.1}_{-0.8}$	84.18	100.31 ± 11.27
	00097199003	60089.0	0.804	$1.46^{+0.14}_{-0.14}$	$8.8^{+1.3}_{-1.1}$	86.1	106.60 ± 12.02
	00097199004	60090.0	0.969	$1.62^{+0.15}_{-0.11}$	$8.8^{+0.8}_{-1.2}$	119.44	142.18 ± 13.86
	00097199005	60091.1	1.004	$1.65^{+0.10}_{-0.19}$	$8.9^{+1.8}_{-0.6}$	92.74	146.15 ± 14.03
	00097199006	60092.1	0.764	$1.35^{+0.13}_{-0.17}$	$8.9^{+1.7}_{-0.9}$	92.47	103.63 ± 11.66
	00097199007	60093.0	0.762	$1.74^{+0.12}_{-0.17}$	$12.3^{+2.1}_{-1.0}$	85.84	123.22 ± 12.78
	00097199008	60094.0	0.782	$1.52^{+0.11}_{-0.08}$	$21.6^{+1.5}_{-2.0}$	233.57	227.68 ± 18.69
	00097199009	60095.6	1.004	$1.47^{+0.06}_{-0.09}$	$27.7^{+2.4}_{-1.3}$	249.49	300.64 ± 22.28
	00097199010	60096.2	0.986	$1.29^{+0.13}_{-0.08}$	$20.4^{+1.3}_{-2.4}$	174.99	232.06 ± 18.06
	00097199011	60097.1	0.984	$1.50^{+0.10}_{-0.10}$	$15.6^{+1.4}_{-1.3}$	157	209.34 ± 17.57
	00097199012	60098.1	0.734	$1.44^{+0.11}_{-0.15}$	$12.5^{+2.0}_{-1.1}$	107.05	146.10 ± 14.05
	00097199013	60099.1	1.349	$1.43^{+0.09}_{-0.11}$	$11.7^{+1.3}_{-0.9}$	177.9	201.01 ± 16.92
	00097199014	60100.0	0.892	$1.53^{+0.14}_{-0.18}$	$7.9^{+1.4}_{-0.9}$	73.04	94.25 ± 1.18
	00097199015	60101.3	0.832	$1.50^{+0.14}_{-0.14}$	$10.7^{+1.4}_{-1.2}$	113.84	120.44 ± 12.54
	00097199016	60102.2	1.184	$1.56^{+0.12}_{-0.11}$	$9.8^{+1.0}_{-1.0}$	115.5	181.46 ± 16.20
XMM-Newton	0920901901	60084.9	7.711	$1.548^{+0.014}_{-0.014}$	$8.22^{+0.12}_{-0.11}$	1622.47	1783.55 ± 59.28

Notes. The net exposure time (t_{exp}) is given in ks, and the unabsorbed flux is given in 10^{-12} erg cm^{-2} s^{-1}.

Appendix B: MWL data

In this appendix, we tabulate the MWL data of this study. The optical data are given in Tables B.1 and B.2, while radio in Table B.3. *Fermi* γ-ray spectrum measurements are given in Table B.4.

Table B.1. Measurements of brightness and linear polarization of S4 0954+65 in optical bands via dedicated observations.

Ins.	Band	MJD	m	σ_m	Π_O	σ_{Π_O}	Ψ_O	σ_{Ψ_O}
NOT	B	60088.944	–	–	13.3%	0.4%	69.3°	0.7°
	B	60092.926	–	–	14.2%	0.3%	72.5°	0.5°
	B	60097.899	–	–	10.8%	0.3%	150.6°	0.6°
	V	60088.948	–	–	13.4%	0.2%	65.9°	0.4°
	V	60092.930	–	–	13.6%	0.2%	69.0°	0.3°
	V	60097.902	–	–	11.6%	0.2%	146.6°	0.3°
	R	60088.939	–	–	13.8%	0.2%	63.1°	0.3°
	R	60092.903	–	–	12.1%	0.1%	64.6°	0.2°
	R	60097.893	–	–	11.9%	0.1%	141.0°	0.2°
	I	60088.941	–	–	14.0%	0.2%	61.4°	0.3°
	I	60092.906	–	–	11.8%	0.1%	63.0°	0.2°
	I	60097.896	–	–	12.4%	0.1%	140.6°	0.3°
T90	B	60074.867	15.92	0.01	–	–	–	–
	B	60075.988	15.31	0.01	–	–	–	–
	V	60074.869	15.25	0.01	–	–	–	–
	V	60075.990	14.73	0.01	–	–	–	–
	R	60065.974	14.70	0.01	–	–	–	–
	R	60067.878	14.13	0.01	36.3%	0.4%	89.6°	0.3°
	R	60074.871	14.71	0.01	–	–	–	–
	R	60075.992	14.21	0.01	–	–	–	–
	I	60074.871	14.01	0.01	–	–	–	–
	I	60075.993	13.55	0.01	–	–	–	–
LX-200	R	60087.898	14.33	0.02	6.5%	0.5%	113.5°	2.1°
	R	60088.887	14.35	0.02	17.87%	0.48%	67.8°	0.8°
	R	60089.913	14.30	0.02	12.70%	0.56%	148.8°	1.3°
	R	60090.900	14.08	0.02	16.09%	0.77%	108.1°	1.4°
	R	60091.901	14.45	0.02	6.15%	0.60%	61.7°	2.8°
	R	60092.906	14.12	0.02	13.83%	0.57%	67.3°	1.2°
	R	60094.898	13.23	0.01	19.21%	0.36%	65.8°	0.6°
	R	60094.917	13.24	0.02	19.28%	0.51%	69.0°	0.8°
	R	60094.929	13.21	0.02	19.89%	0.44%	72.5°	0.7°
	I	60087.910	13.69	0.02	–	–	–	–
	I	60088.903	13.65	0.01	–	–	–	–
	I	60089.944	13.63	0.03	–	–	–	–
	I	60090.886	13.42	0.02	–	–	–	–
	I	60091.913	13.80	0.01	–	–	–	–
	I	60092.917	13.48	0.01	–	–	–	–
	I	60094.907	12.64	0.01	–	–	–	–
RoboPol	R	60082.835	14.28	0.02	13.98%	0.12%	149.0°	0.3°
	R	60082.842	14.29	0.02	13.22%	0.16%	150.1°	0.4°
	R	60083.802	14.13	0.02	10.40%	0.10%	143.0°	0.3°
	R	60104.818	14.12	0.02	13.48%	0.10%	154.2°	0.2°
	R	60105.811	13.95	0.02	27.09%	0.10%	176.5°	0.1°
	R	60106.824	13.87	0.02	17.02%	0.09%	164.5°	0.2°

Notes. "Ins." represents the instrument or telescope facility employed (see Sect. 3). "Band" gives the optical band. m and σ_m refer to the brightness and its error in magnitudes, respectively. Π_O and σ_{Π_O} give the optical polarization degree and its error, respectively. Ψ_O and σ_{Ψ_O} represent the optical polarization angle and its error, respectively. All errors are 1σ Gaussian. For brevity, in case of several equivalent (within 1σ) brightness entries per one night, only one one of them is shown.

Table B.2. Measurements of brightness of S4 0954+65 in the optical band via all-sky surveys.

Survey	Band	MJD	m	σ_m
ZTF	r	60082.199	14.51	0.02
	r	60084.197	14.26	0.02
	r	60097.221	13.71	0.02
	r	60099.240	14.57	0.02
ATLAS	o	60082.325	14.59	0.01
	o	60084.291	14.36	0.02
	o	60086.262	14.77	0.03
	o	60088.274	14.11	0.03
	o	60090.297	14.67	0.02
	o	60092.295	14.69	0.03
	o	60094.282	13.72	0.01
	o	60096.265	13.88	0.02
	o	60098.295	14.20	0.03
	o	60100.284	14.99	0.06
	o	60102.263	15.04	0.02

Notes. "Survey" represents the all-sky survey used (see Sect. 3). "Band" gives the optical band of the measurements. m and σ_m refer to the brightness and its 1σ Gaussian error in magnitudes, respectively.

Table B.3. Linear polarization measurements of S4 0954+65 in radio bands.

Program	ν (GHz)	MJD	Π_R	Ψ_R
QUIVER	4.8	60093.5	(2.43 ± 0.47)%	60.0° ± 2.4°
QUIVER	4.8	60097.7	(1.40 ± 0.54)%	61.9° ± 3.1°
QUIVER	10	60088.8	(0.68 ± 0.15)%	61.0° ± 6.5°
QUIVER	10	60093.5	(1.65 ± 0.08)%	55.8° ± 2.2°
QUIVER	10	60097.7	(1.08 ± 0.09)%	57.9° ± 2.3°
QUIVER	17	60093.5	(2.53 ± 0.22)%	37.0° ± 2.2°
QUIVER	17	60097.7	(1.92 ± 0.28)%	50.1° ± 2.2°
SMAPOL	225.5	60094.2	(3.16 ± 0.39)%	115.73° ± 1.99°
SMAPOL	225.5	60099.3	(4.05 ± 0.50)%	115.90° ± 1.97°

Table B.4. *Fermi* γ-ray spectrum in the 0.1-100 GeV band.

Frequency (ν) (1)	νF_ν (2)	Error of νF_ν (3)
22.7	7.1	1.1
23.1	11.1	1.3
23.5	8.2	1.5
24.0	5.2	2.1
24.4	< 2.7	–
24.8	< 5.4	–
25.3	< 9.8	–

Notes. Column (1) gives frequency in log(Hz) units, column (2) gives the frequency multiplied by the flux density per frequency (νFν) in units of 10^{-11} erg s^{-1} cm^{-2}, and column (3) gives the error of the values in column (2).